

*2006 IEEE NSREC
Short Course*

Section I:

Modeling the Space Radiation Environment

Michael Xapsos
NASA Goddard Space Flight Center
Greenbelt, MD 20771

Approved for public release; distribution is unlimited

Modeling the Space Radiation Environment

Michael Xapsos, NASA Goddard Space Flight Center
NSREC 2006 Short Course

Outline

I.	Introduction.....	2
II.	The Solar Activity Cycle	3
III.	The Earth's Trapped Radiation Environment.....	5
	A. The Magnetosphere and Trapped Particle Motion.....	5
	B. Characteristics of Trapped Protons.....	8
	C. The AP-8 Model	9
	D. Recent Developments in Trapped Proton Models	12
	E. Characteristics of Trapped Electrons	18
	F. The AE-8 Model	19
	G. Recent Developments in Trapped Electron Models	20
IV.	Galactic Cosmic Rays.....	29
	A. General Characteristics	29
	B. Galactic Cosmic Ray Models.....	32
V.	Solar Particle Events	35
	A. General Characteristics	35
	B. Solar Proton Models	37
	1. The Maximum Entropy Principle and the Distribution of Solar Proton Event Magnitudes	37
	2. Cumulative Fluence During Solar Maximum.....	39
	3. Cumulative Fluence During Solar Minimum	42
	4. Extreme Value Theory and Worst Case Events.....	44
	5. Self-Organized Criticality and the Nature of the Energy Release Process	48
	a) Rescaled Range Analysis.....	49
	b) Fractal Behavior.....	52
	c) Power Function Distribution.....	53
	C. Solar Heavy Ion Models	54
VI.	Future Challenges	56
VII.	References.....	57

I. Introduction

There are a number of environmental hazards that spacecraft must be designed for, which includes low energy plasma, particle radiation, neutral gas particles, ultraviolet and x-ray radiation, micrometeoroids and orbital debris. This manuscript is focused on hazards present for devices and integrated circuits in the space environment. Hence it is mainly concerned with three categories of high-energy particle radiations in space. The first is particles trapped by planetary magnetic fields such as the earth's Van Allen Belts. The second is the comparatively low-level flux of ions that originate outside of our solar system called galactic cosmic rays. The third is bursts of radiation emitted by the sun, characterized by high fluxes of protons and heavy ions, referred to as solar particle events.

In order to have reliable, cost-effective designs and implement new space technologies, the radiation environment must be understood and accurately modeled. Underestimating the radiation levels leads to excessive risk and can result in degraded system performance and loss of mission lifetime. Overestimating the radiation levels can lead to excessive shielding, reduced payloads, over-design and increased cost.

The last approximately 10 years has been a renaissance period in space radiation environment modeling for a number of reasons. There has been a growing need for some time now to replace the long-time standard AP-8 and AE-8 radiation belt models. These are based on data that badly needed to be updated. A growing number of interplanetary exploration initiatives, particularly manned initiatives to the moon and Mars, are driving the development of improved models of the galactic cosmic ray and solar particle event environments. Improved radiation detectors and other technologies such as those operating on the Advanced Composition Explorer (ACE) and the Solar, Anomalous and Magnetospheric Particle EXplorer (SAMPEX) satellites have led to unprecedented measurement accuracy and resolution of space radiation properties. Finally, the pervasive use of commercial-off-the-shelf (COTS) microelectronics in spacecraft to achieve increased system performance must be balanced by the need to accurately predict their complex responses in space.

The main objective of this section of the short course is to present recent developments in modeling the trapped particle, galactic cosmic ray and solar particle event radiation environments for radiation effects applications. This will start with background information and initial reviews of the traditional models before proceeding to the newer models. In the case of solar particle event models a number of probabilistic methods not commonly found in the literature have recently been applied. An overview of the origins and backgrounds of these methods will be given leading up to the environment applications. Comparisons between various models will be shown for different phases of the solar cycle and for missions ranging from low earth orbit out to interplanetary space.

As galactic cosmic rays and solar particles enter and interact with the earth's upper atmosphere, showers of secondary particles are produced. Secondary neutrons are the most important contributor to single event effects at altitudes below about 60,000 feet. Discussions of the atmospheric and terrestrial neutron environments can be found elsewhere [Ba97], [Ba05].

II. The Solar Activity Cycle

The sun is both a source and a modulator of space radiations. Understanding its cyclical activity is an important aspect of modeling the space radiation environment. The solar activity cycle is approximately 11 years long. During this period there are typically 7 years during solar maximum when activity levels are high and 4 years during solar minimum when activity levels are low. In reality the transition between solar maximum and solar minimum is a continuous one but it is often considered to be abrupt for convenience. At the end of each 11-year cycle the magnetic polarity of the sun reverses and another 11-year cycle follows. Thus, strictly speaking the total activity cycle is approximately 22 years long. Of the space radiations considered here the magnetic polarity apparently only affects the galactic cosmic ray fluxes [Ba96a], and not the trapped particle or solar particle event fluxes. Thus, things are often viewed on an approximately 11-year cyclical basis.

Two common indicators of this approximately 11-year periodic solar activity are sunspot numbers and solar 10.7 cm radio flux ($F_{10.7}$). The most extensive record is that of observed sunspot numbers, which dates back to the 1600s. This record is shown in Figure 1. The numbering of sunspot cycles began in 1749 and it is currently near the end of solar cycle 23. The record of $F_{10.7}$ began part way through solar cycle 18 in the year 1947 and is shown in Fig. 2.

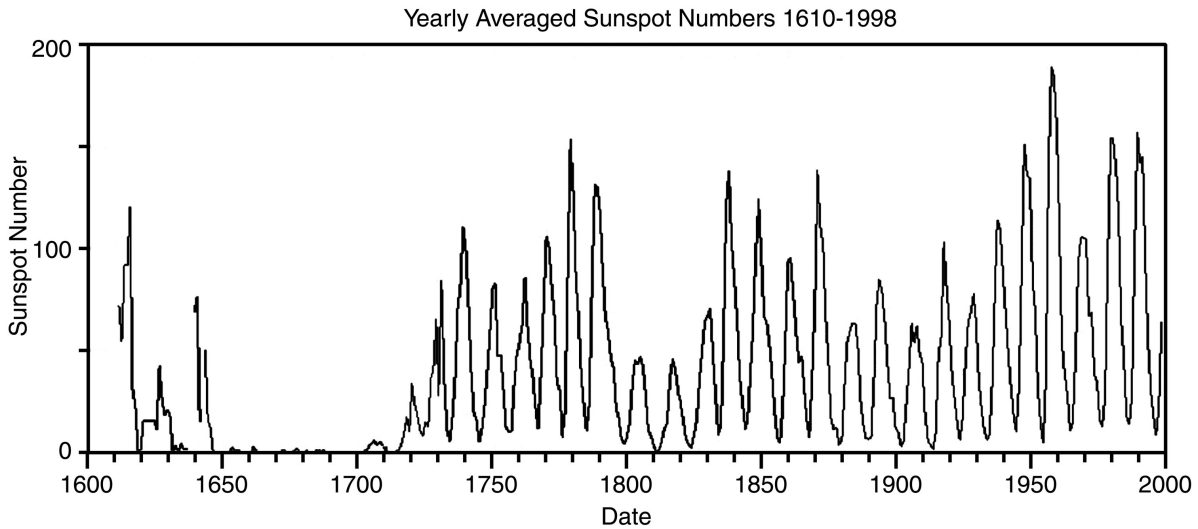


Figure 1. The observed record of yearly averaged sunspot numbers.

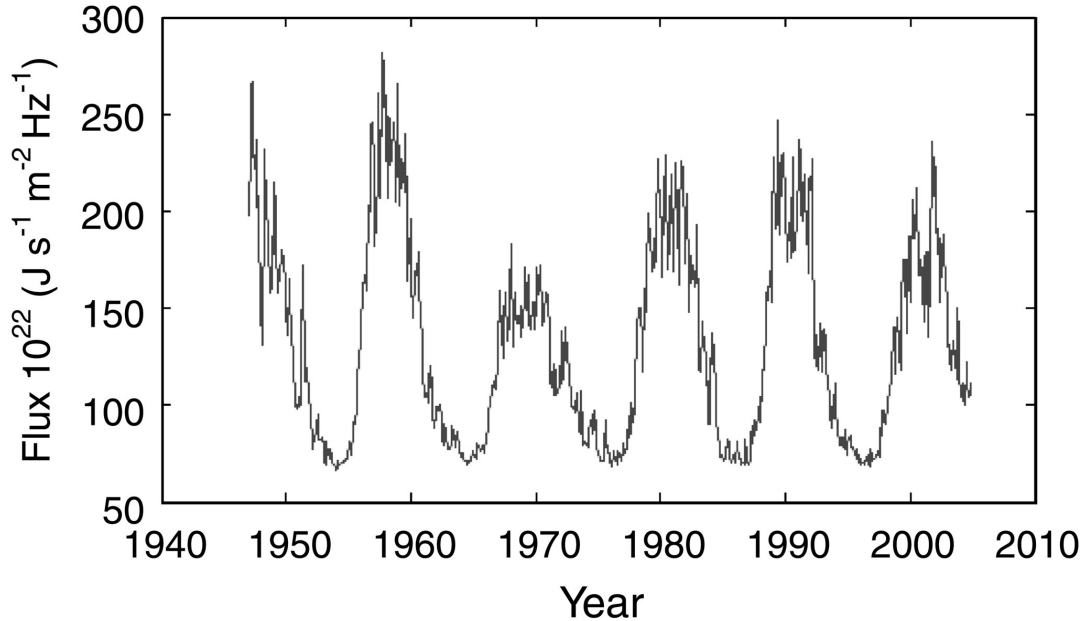


Figure 2. Measured values of solar 10.7 cm radio flux.

Although sunspot numbers and $F_{10.7}$ are commonly accepted indicators of solar activity, quantitative relations to measured radiation events and fluxes are not necessarily straight forward. Solar particle events are known to occur with greater frequency and intensity during the declining phase of solar maximum [Sh95]. Trapped electron fluxes also tend to be higher during the declining phase [Bo03]. Trapped proton fluxes in low earth orbit (LEO) reach their maximum during solar minimum but exactly when this peak is reached depends on the particular location [Hu98]. Galactic cosmic ray fluxes are also at a maximum during solar minimum but in addition depend on the magnetic polarity of the sun [Ba96a].

There has been considerable effort put into forecasting long-term solar cycle activity. A review of a number of the methods is presented by Hathaway [Ha99]. These include regression methods, which involve fitting a function to the data as the cycle develops. Also discussed are precursor methods, which estimate the amplitude of the next cycle based on some type of correlation with prior information. These methods can also be combined. In addition, physically based methods are being developed based on the structure of the magnetic field within the sun and heliosphere [Sc96], [Di06].

However, accurate methods for predicting future solar cycle activity levels prior to the start of the cycle have thus far been elusive. A potential breakthrough, however, has recently been reported that uses a combination of computer simulation and observations of the solar interior from instrumentation onboard the Solar and Heliospheric Observatory (SOHO) [Di06]. Given the current state of this modeling, probabilistic models of solar activity can be useful. Such a model of $F_{10.7}$ is shown in Figure 3 [Xa02]. This also illustrates the general behavior of the observed cyclical properties, at least over recent cycles. The greater the peak activity of a cycle, the faster the rise-time to the peak level. Furthermore the cyclical activity is asymmetric such that the descending phase of the cycle is longer than the ascending phase.

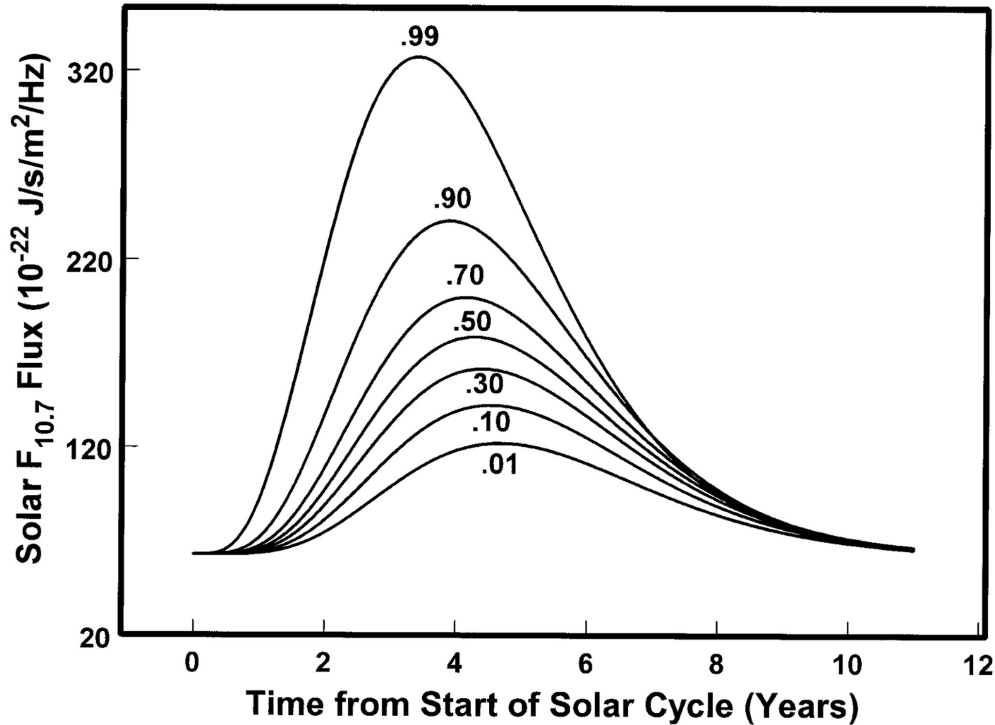


Figure 3. Probabilistic model of $F_{10.7}$. The various curves are labeled as a function of confidence level that the activity shown will not be exceeded [Xa02].

III. The Earth's Trapped Radiation Environment

This section leads up to recent modeling developments for trapped protons and trapped electrons geared toward radiation effects applications. Initially a review of background information and related physical processes will be given. Further background information can be found in [Ba97], [Ma02] and [Wa94].

A. The Magnetosphere and Trapped Particle Motion

The earth's magnetosphere consists of both an external and an internal magnetic field. The external field is the result of plasma or ionized gas that is continually emitted by the sun called the solar wind. The internal or geomagnetic field originates primarily from within the earth and is approximately a dipole field. As shown in Figure 4, the solar wind and its embedded magnetic field tends to compress the geomagnetic field. During moderate solar wind conditions, the magnetosphere terminates at roughly 10 earth radii on the sunward side. During turbulent magnetic storm conditions it can be compressed to about 6 earth radii. The solar wind generally flows around the geomagnetic field and consequently the magnetosphere stretches out to a distance of possibly 1000 earth radii in the direction away from the sun.

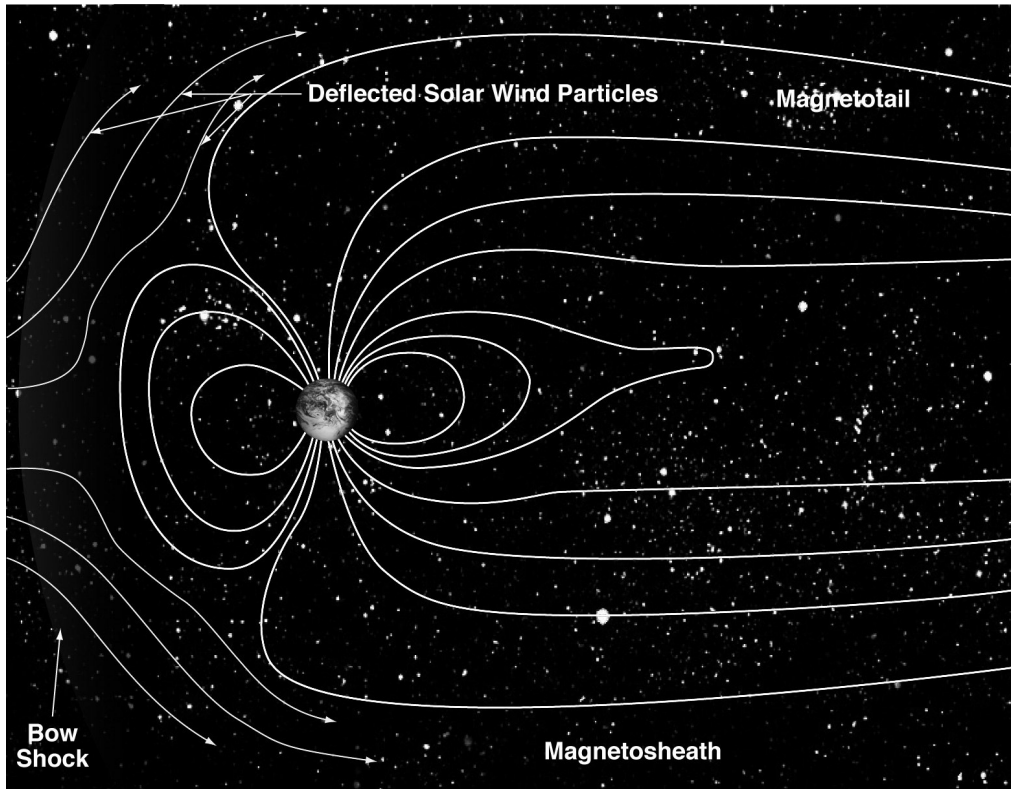


Figure 4. The earth's magnetosphere.

Figure 5 shows the geomagnetic field, which is approximately dipolar for altitudes of up to about 4 or 5 earth radii. It turns out that the trapped particle populations are conveniently mapped in terms of the dipole coordinates approximating the geomagnetic field. This dipole coordinate system is not aligned with the earth's geographic coordinate system. The axis of the magnetic dipole field is tilted about 11 degrees with respect to the geographic North-South axis and its origin is displaced by a distance of more than 500 km from the earth's geocenter. The standard method is to use McIlwain's (B, L) coordinates [Mc61]. Within this dipole coordinate system, L represents the distance from the origin in the direction of the magnetic equator, expressed in earth radii. One earth radius is 6371 km. B is simply the magnetic field strength. It describes how far away from the magnetic equator a point is along a magnetic field line. B -values are a minimum at the magnetic equator and increase as the magnetic poles are approached.

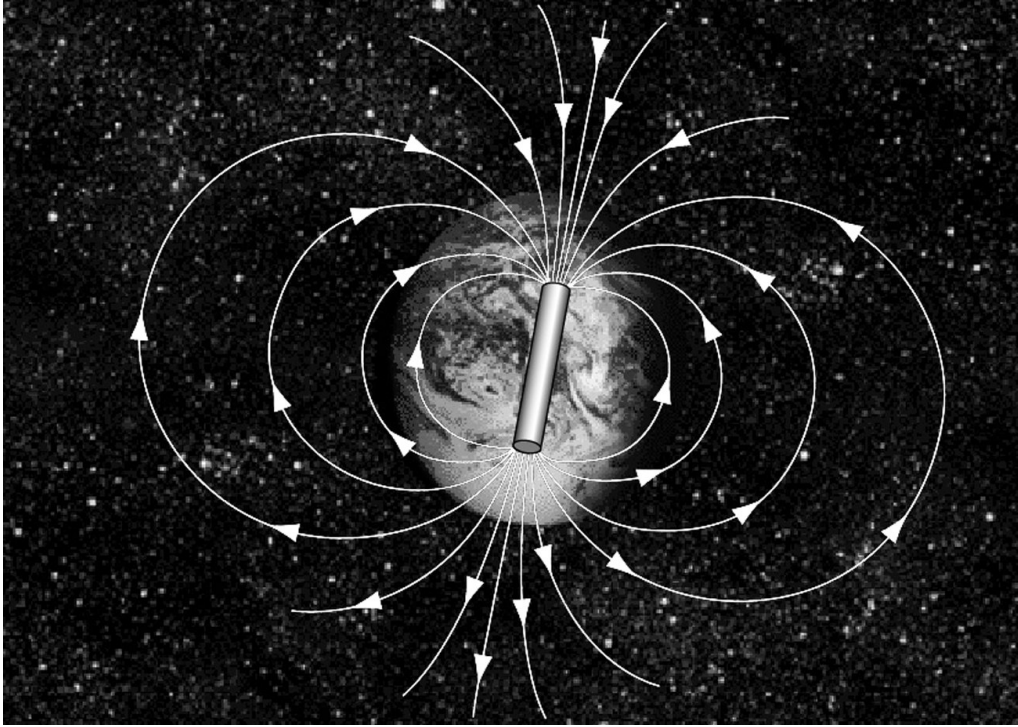


Figure 5. The internal magnetic field of the earth is approximately a dipole field.

Next the basic motion of a trapped charged particle in this approximately dipole field will be discussed. Charged particles become trapped because the magnetic field can constrain their motion. As shown in Figure 6 the motion a charged particle makes in this field is to spiral around and move along the magnetic field line. As the particle approaches the polar regions the magnetic field strength increases and causes the spiral to tighten. Eventually the field strength is sufficient to force the particle to reverse direction. Thus, the particle is reflected between so called “mirror points” and “conjugate mirror points”. Additionally there is a slower longitudinal drift of the path around the earth that is westward for protons and eastward for electrons. Once a complete azimuthal rotation is made around the earth, the resulting toroidal surface that has been traced out is called a drift shell. A schematic of such a drift shell is shown in Figure 7.

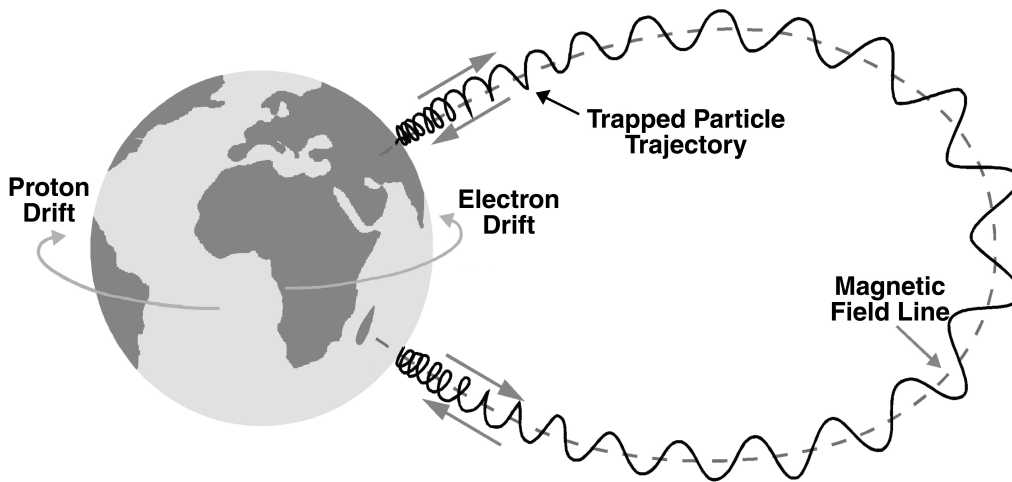


Figure 6. Motion of a charged trapped particle in the earth's magnetic field.

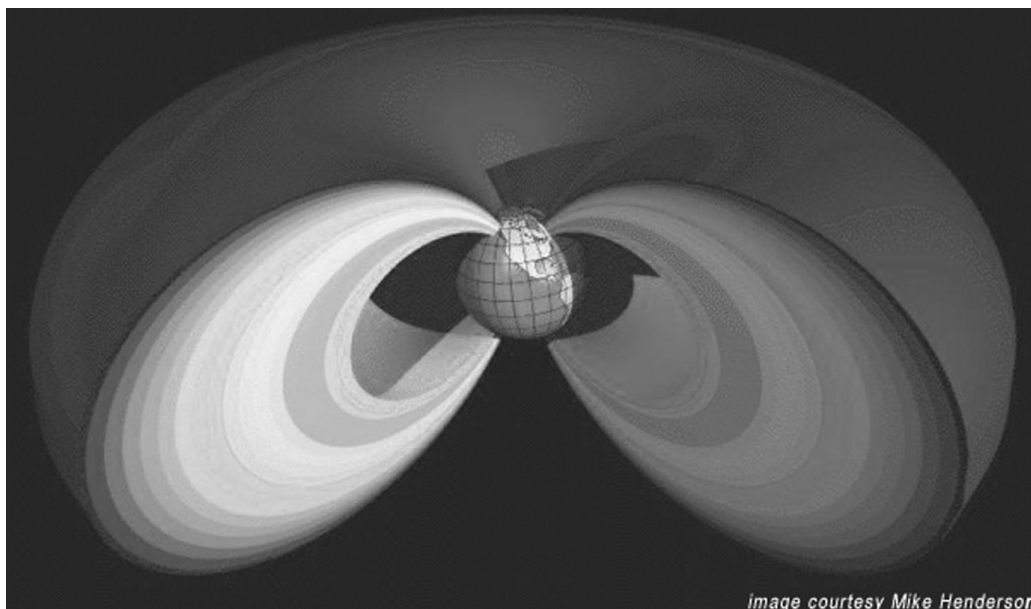


Figure 7. Illustration of the geometry of drift shells.

B. Characteristics of Trapped Protons

Some of the characteristics of trapped protons and their radiation effects are summarized in Table 1. The L -shell range is from $L = 1.15$ at the inner edge of the trapped environment out beyond geosynchronous orbits to an L -value of about 10. Trapped proton energies extend up to a few 100's of MeV, at which point the fluxes begin to fall off rapidly. The energetic trapped proton population with energies > 10 MeV is confined to altitudes below 20,000 km, while

protons with energies of about 1 MeV or less are observed at geosynchronous altitudes and beyond. The maximum flux of energetic protons occurs at an L -value of around 1.8 and exceeds 10^5 p/(cm²-s). Close to the inner edge, proton fluxes are modulated by the atmospheric density. They can decrease by as much as a factor of 2 to 3 during solar maximum due to atmospheric expansion and resulting losses caused by scattering processes.

Trapped protons can cause Total Ionizing Dose (TID) effects, Displacement Damage (DD) effects and Single Event Effects (SEE). The metric used for TID studies is ionizing dose, defined as the energy deposited per unit mass of material that comprises the sensitive volume. The unit commonly employed is the “rad” where 1 rad = 100 erg/g. One metric for proton-induced displacement damage is to use the equivalent fluence of a given proton energy, often taken as 10 MeV [An96]. A quantity analogous to the ionization dose, called the displacement damage dose (DDD), is also used to study displacement effects in materials [Ma99], [Wa04]. It is defined as the energy that goes into displaced atoms per unit mass of material that comprises the sensitive volume. The units are analogous to ionizing dose except that it is the nonionizing component. Finally, it is noted that studies of proton-induced SEE commonly use the proton energy incident on the sensitive device volume as a relevant parameter. Most proton-induced SEE occur as a result of target recoil products that result from interactions with the incident proton. The incident proton energy has a significant influence on these products and that is the reason why results are commonly presented in terms of it.

Table 1. Trapped Proton Characteristics.

L -Shell Values	Energies	Fluxes* (>10 MeV)	Radiation Effects	Metrics
1.15 – 10	Up to 100’s of MeV	Up to $\sim 10^5$ cm ⁻² s ⁻¹	Total Ionizing Dose (TID); Displacement Damage (DD); Single Event Effects	Dose for TID; 10 MeV equivalent fluence and Displacement Damage Dose for DD

* long-term average

C. The AP-8 Model

The well-known AP-8 trapped proton model is the eighth version of a model development effort led by James Vette. Over the years these empirical models have been indispensable for spacecraft designers and for the radiation effects community in general. The trapped particle models are static maps of the particle population during solar maximum and solar minimum. They are mapped in a dipole coordinate system such as the (B,L) coordinates described in section IIIA. A spacecraft orbit is calculated with an orbit generator. The orbit coordinates are then transformed to (B,L) coordinates and the trapped particle radiation environment determined. Models such as this are implemented in the SPace ENVironment Information System (SPENVIS) suite of programs [http]. Details of the AP-8 model and its predecessors can be found in [Sa76], [Ve91] and [Ba97].

Figure 8 is a contour plot of the trapped proton population with energies > 10 MeV shown in a dipole coordinate system. The x-axis is the radial distance along the geomagnetic equator in units of earth-radii while the y-axis is the distance along the geodipole axis, also in units of earth-radii. Thus, a y-value of zero represents the geomagnetic equator [Da96]. A semi-circle with a radius of one centered at the point (0,0) represents the earth's surface on this plot. It is seen that it is a particularly convenient way to reduce a large quantity of information and get an overview of the particle population on a single plot.

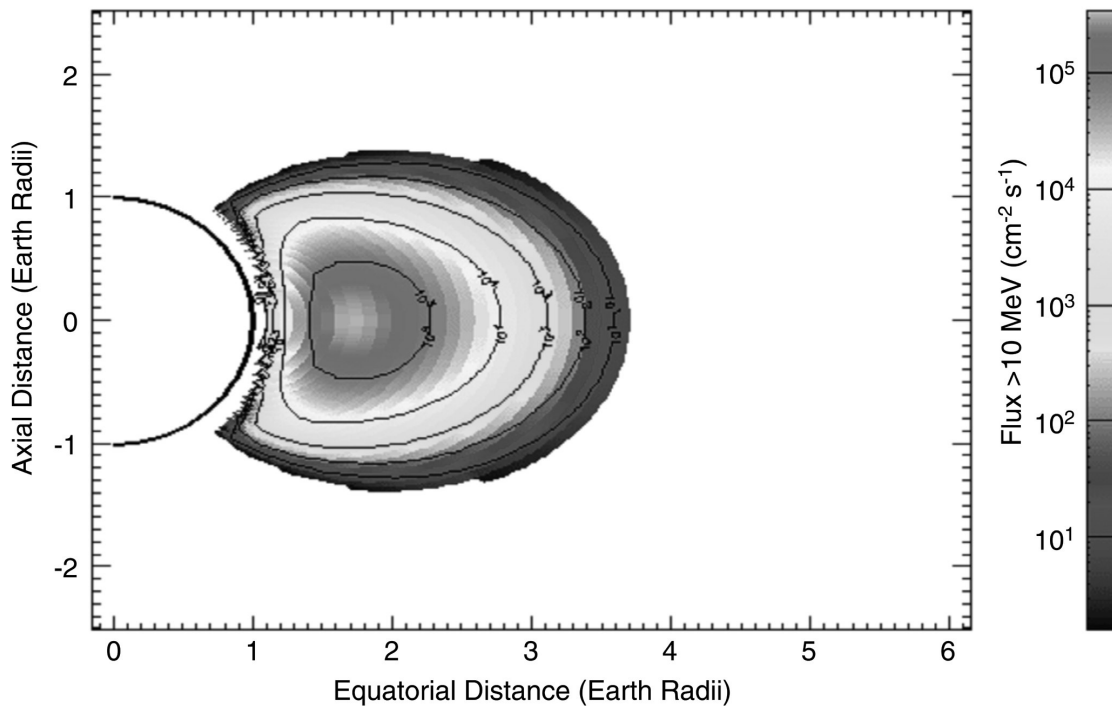


Figure 8. The trapped proton population with energies > 10 MeV as predicted by the AP-8 model for solar maximum conditions. From SPENVIS, [http].

For spacecraft that have an orbit lower than about 1000 km the so-called “South Atlantic Anomaly” (SAA) dominates the radiation environment. This anomaly is due to the fact that the earth's geomagnetic and rotational axes are tilted and shifted relative to each other as discussed in section IIIA. Thus, part of the inner edge of the proton belt is at lower altitudes as shown in Figure 9. This occurs in the geographic region south and east of Brazil. It is shown in Figure 10 as a contour plot on geographic coordinates for > 10 MeV proton fluxes at a 500 km altitude.

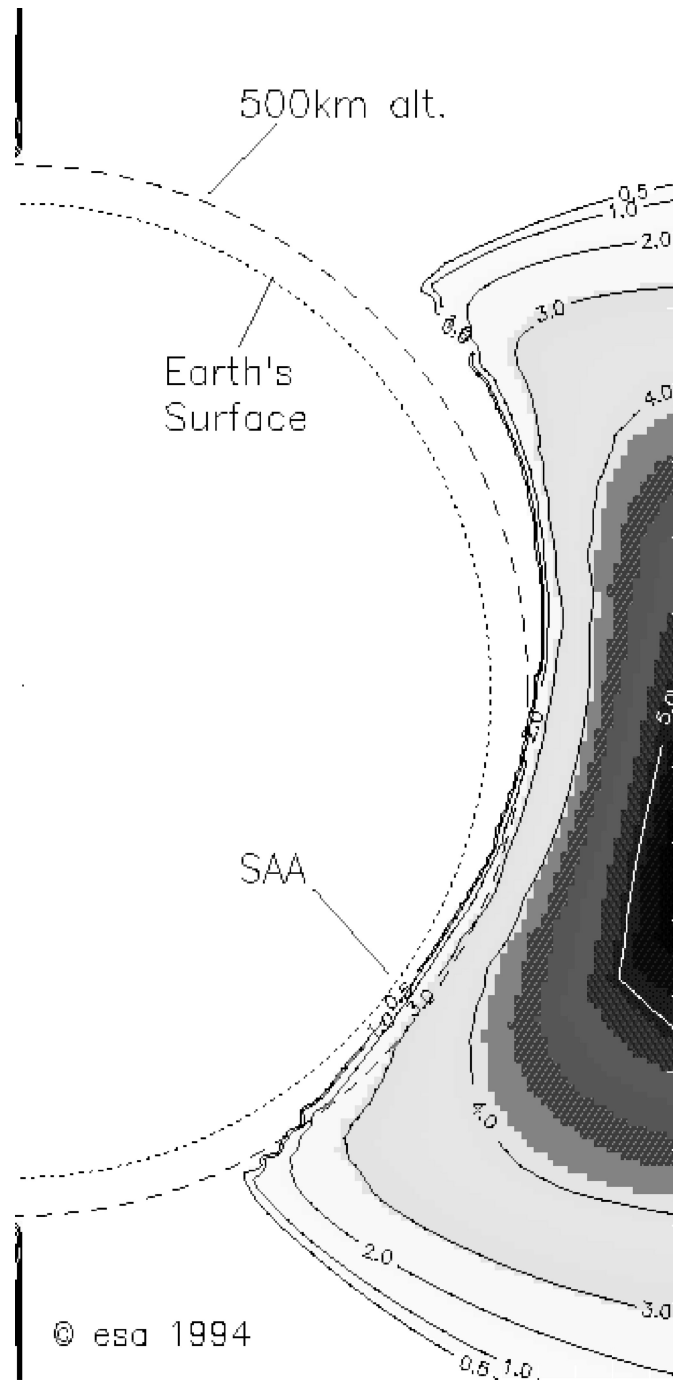


Figure 9. The South Atlantic Anomaly [Da96].

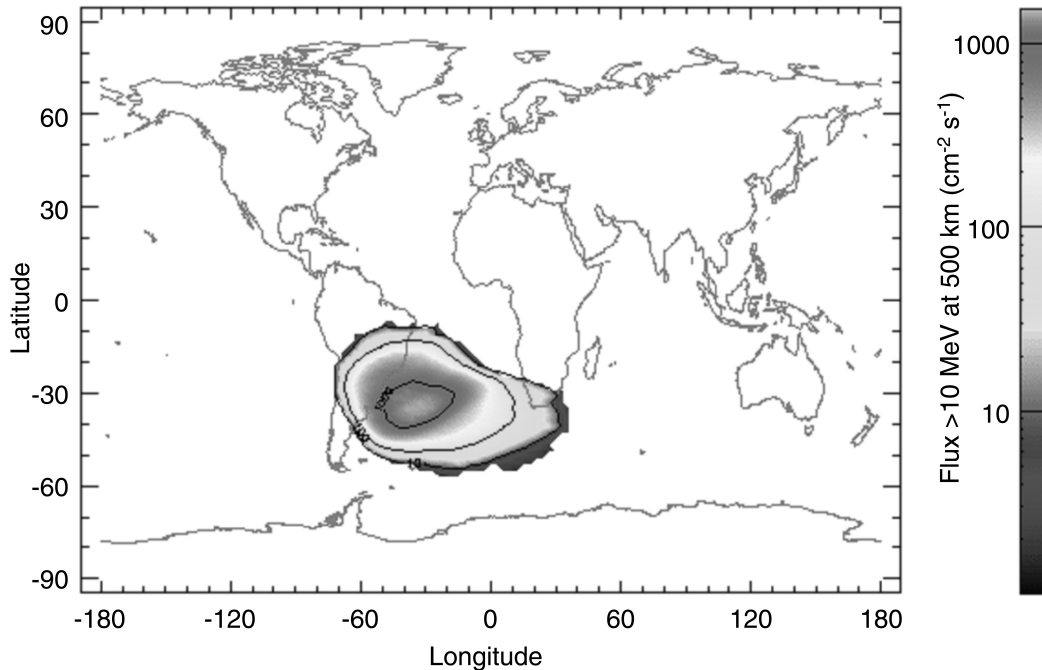


Figure 10. Contour plot of proton fluxes > 10 MeV in the SAA at a 500 km altitude during solar maximum. From SPENVIS, [http].

The main difference between the solar maximum and solar minimum maps is seen at low altitudes where the fluxes are less during solar maximum. The reason is that the atmosphere expands as a result of heating during solar maximum so that trapped protons are lost due to scattering processes at a higher rate.

D. Recent Developments in Trapped Proton Models

This section discusses some of the measurements and modeling efforts that have been performed in an attempt to provide a more updated and dynamic description of the trapped proton population. The advantages of the AP-8 model are its long heritage of use and rather complete description of trapped protons in terms of energies and geographic location. However, it is based on data that were taken mainly in the 1960's and early 1970's. Thus a serious concern is whether it still accurately represents the trapped proton environment today.

The PSB97 model, developed at the Belgian Institute for Aeronomy (BIRA) and the Aerospace Corporation, is a LEO model for the solar minimum time period [He99]. It is based on the Proton/Electron Telescope (PET) onboard SAMPEX. A notable feature of this model is its broad proton energy range, which extends from 18.5 to 500 MeV.

One of the significant extensions of this model beyond AP-8 is that it accounts for secular variation of the geomagnetic field. This variation results because the center of the geomagnetic dipole field drifts away from the geocenter of the Earth at about 2.5 km per year and the magnetic moment decreases with time [http]. The overall effect is to draw the SAA slowly inward toward the earth. A comparison of measurements of the SAA made for > 18.5 MeV protons at an altitude of 500 km is shown in Figure 11 [He99]. It is seen that compared to the AP-8 model of magnetic field epoch 1960, the PSB97 model of magnetic field epoch 1995

shows that the SAA has a higher peak flux value that has drifted westward. It also indicates the SAA covers a broader geographic region.

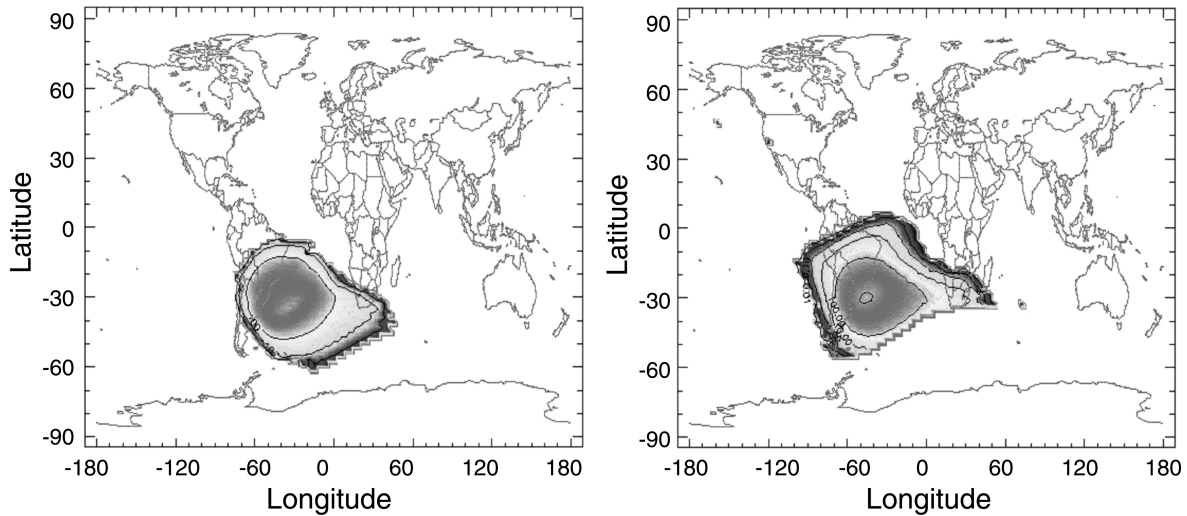


Figure 11. Comparison of the SAA during solar minimum for > 18.5 MeV protons at a 500 km altitude for the time period of the AP-8 model (left) and for the modern SAMPEX/PET measurements (right) [He99].

The Low Altitude Trapped Radiation Model (LATRM), formerly called NOAAPRO, is a LEO proton model developed at the Boeing Company [Hu98]. It is based on 17 years of data taken by the TIROS/NOAA satellites. It accounts for the secular variation of the geomagnetic field using an internal field model. One of the important new features of this model was to account for a continuous solar cycle variation of the trapped proton flux as opposed to AP-8, which transitions discontinuously between the solar maximum and solar minimum periods. This was done using $F_{10.7}$ as a proxy for the atmospheric density, which controls the proton flux at low altitudes. Figure 12 shows the proton flux for different L -values superimposed upon $F_{10.7}$ for the period of time the model is based on. It is seen that the flux is anti-correlated with $F_{10.7}$ due to the greater losses of protons to the atmosphere during solar maximum. The proton flux also shows a phase lag that is dependent on L . Using these empirical relations, the LATRM is able to describe the trapped proton variations over the complete solar cycle as well as make projections into the future.

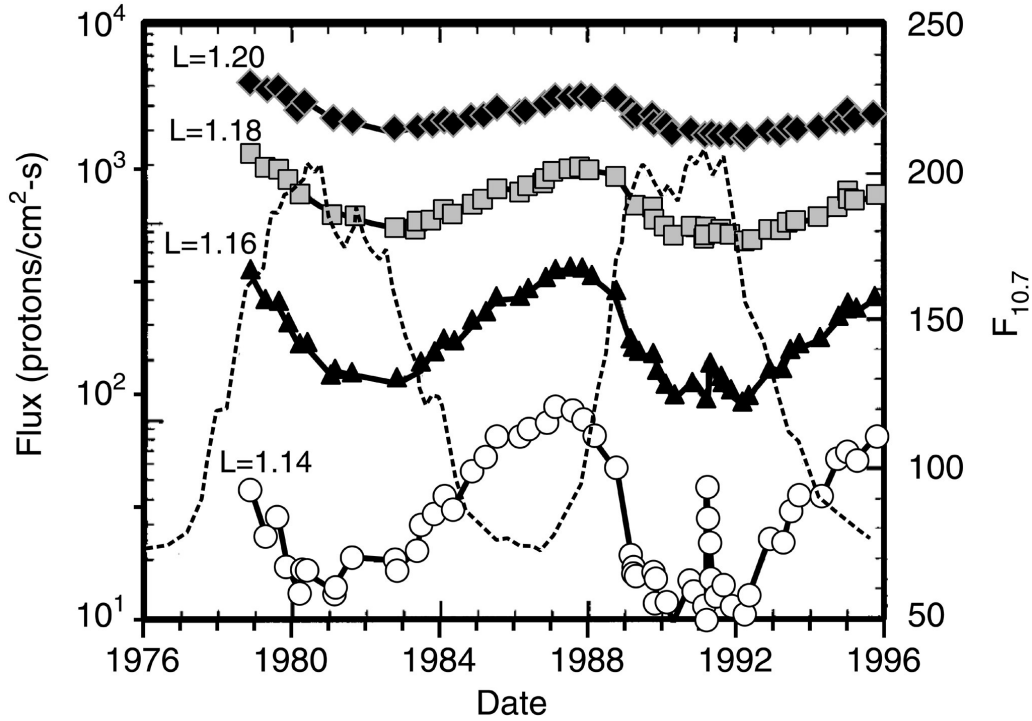


Figure 12. Comparison of the trapped proton flux (points) for low L -values to $F_{10.7}$ (dotted curve) [Hu98].

The Combined Release and Radiation Effects Satellite PROton (CRRESPRO) trapped proton model is based on data collected for a 14-month period during solar maximum of solar cycle 22 [Gu96]. Although the population of trapped protons in the region of the inner belt is fairly stable, measurements from this satellite demonstrated significant temporal and spatial variability of trapped particles. In particular it showed that the greatest time variations of trapped protons occur in Medium Earth Orbit (MEO). CRRESPRO consists of both a quiet and an active model of trapped protons during solar maximum ranging from L -values of 1.15 to 5.5. The quiet model is for the mission period prior to a large geomagnetic storm that occurred in March 1991 and the active model is for the mission period afterward. Figure 13 shows the CRRESPRO quiet and active models along with AP-8, demonstrating the formation of a second, stable proton belt for L -values between 2 and 3. The belt was particularly apparent in the 20 to 70 MeV energy range [Gu96]. Although the flux levels began to decay immediately they were still measurable on the Russian METEOSAT after about 2 years [Di97].

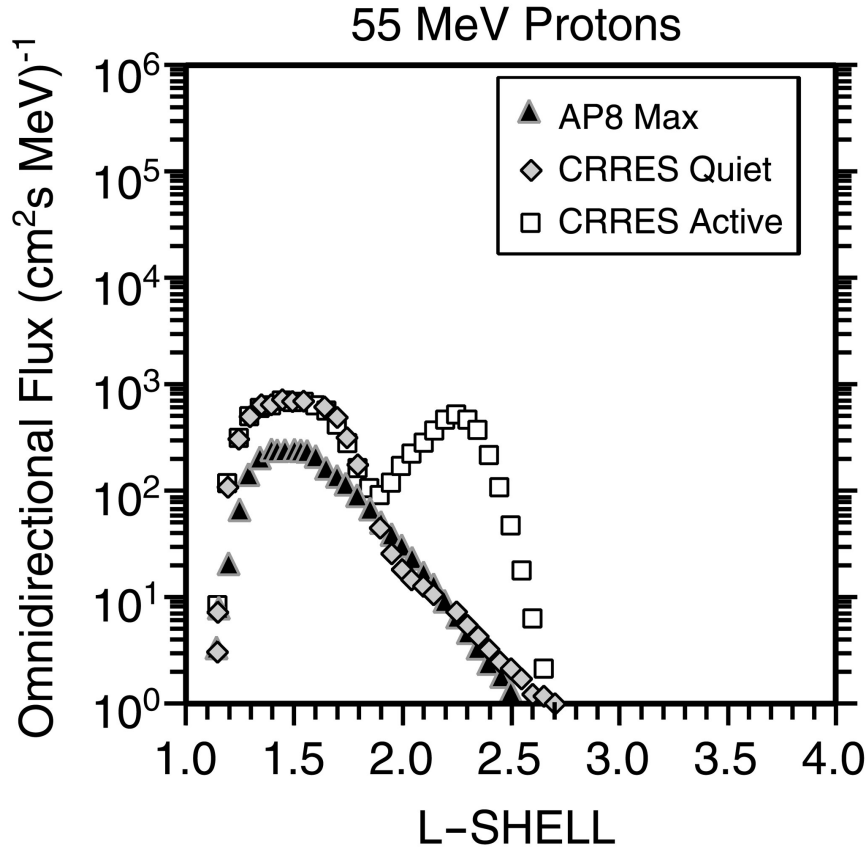


Figure 13. CRESSPRO quiet and active models compared to AP-8 for 55 MeV differential proton fluxes [Gu96].

Recently, the Trapped Proton Model-1 (TPM-1) was developed by Huston [Hu02]. This model combines many of the features of LATRM and CRESSPRO. It covers the geographic region from about 300 km out to nearly geosynchronous orbit for protons in the 1.5 to 81.5 MeV energy range. It models the continuous variation of fluxes over the solar cycle, and also contains a model of both quiet and active conditions as observed onboard CRRES. TPM-1 has a time resolution of 1 month, which is a significant improvement over AP-8. The AP-8 model should be used only for long-term average fluxes.

As discussed above, the TPM-1 and PSB97 models have a number of advantages over the AP-8 model. In addition, these models are based on relatively modern instrumentation compared to AP-8. Thus, it is interesting to examine how representative the AP-8 model is of the current trapped proton environment. Figure 14 shows a comparison of the fluxes calculated for an orbit similar to the International Space Station for TPM-1 (quiet conditions), PSB97 and AP-8. All results are for the solar minimum time period. Comparing TPM-1 to AP-8 it is clear there is a significant difference in the hardness of the energy spectra. TPM-1 calculates lower fluxes than AP-8 for low energies and higher fluxes for high energies. Examining the results calculated with PSB97, it is seen that the overlap with the TPM-1 model in their common energy range of about 20 to 80 MeV is excellent. Thus, it would appear that significant discrepancies now exist with the AP-8 model for LEO. A combination of TPM-1 and PSB97, including an update of data

taken with the SAMPEX/PET instrument, would result in a fairly complete trapped proton model.

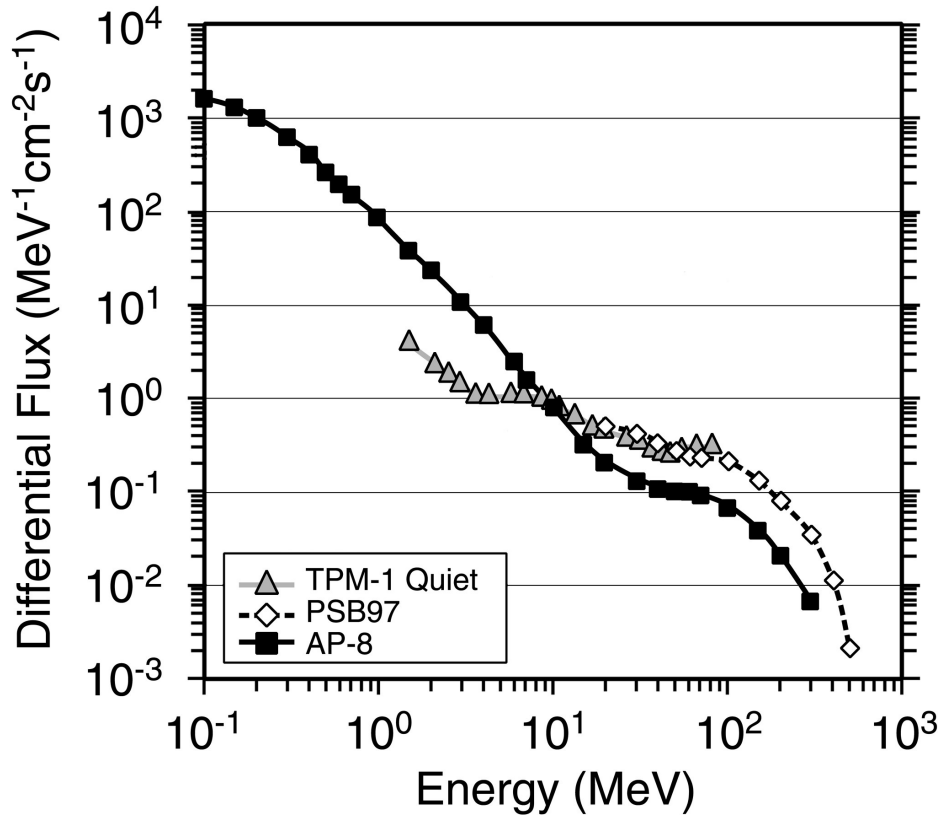


Figure 14. Comparison of fluxes predicted by three trapped proton models for an orbit similar to the International Space Station during solar minimum [La05].

Figures 15 and 16 are comparisons of the TPM-1 and CRRESPRO models, both quiet and active, and the AP-8 model for solar maximum conditions. This comparison is for a 2000 km x 26,750 km elliptical orbit with a 63.4 degree inclination. In this case it is seen that AP-8 predicts significantly higher fluxes over nearly the full energy spectrum, although the difference is less for the TPM-1 active calculation. It can be seen from the examples discussed in this section that these type of comparisons are highly orbit dependent and must be considered on a case-by-case basis. An excellent summary of a number of model comparisons for common orbits is given in Lauenstein and Barth [La05].

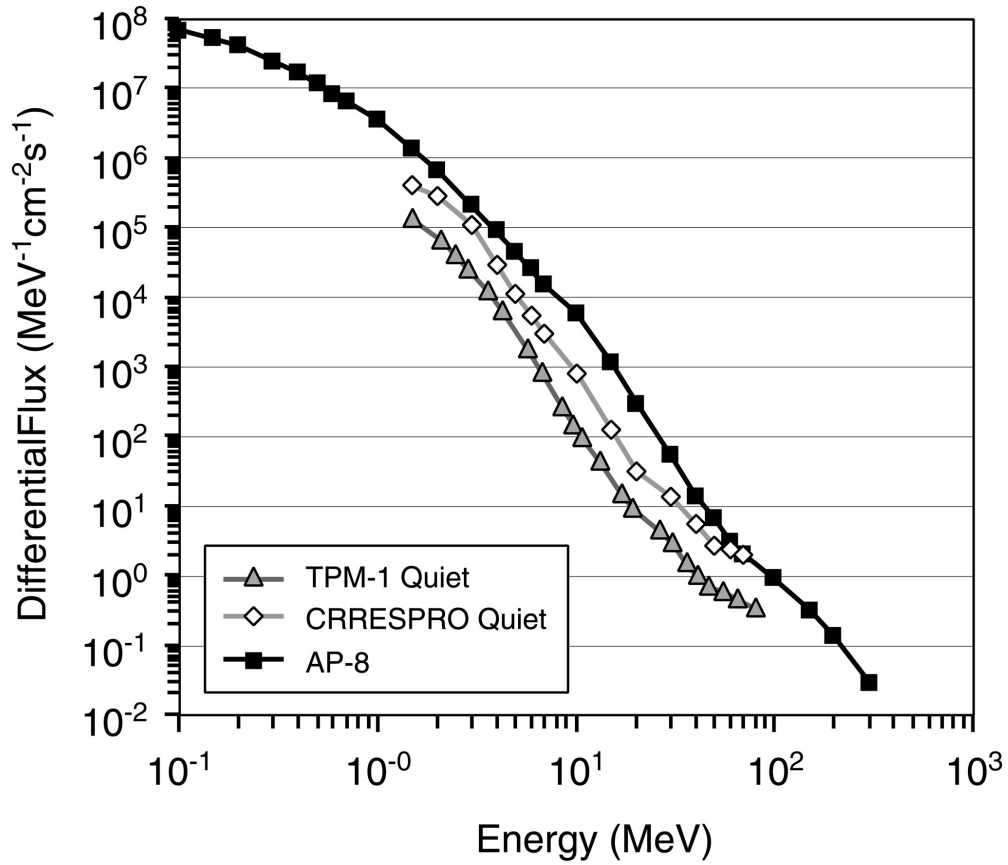


Figure 15. Comparison of trapped proton models for an elliptical orbit during quiet conditions and the solar maximum time period [La05].

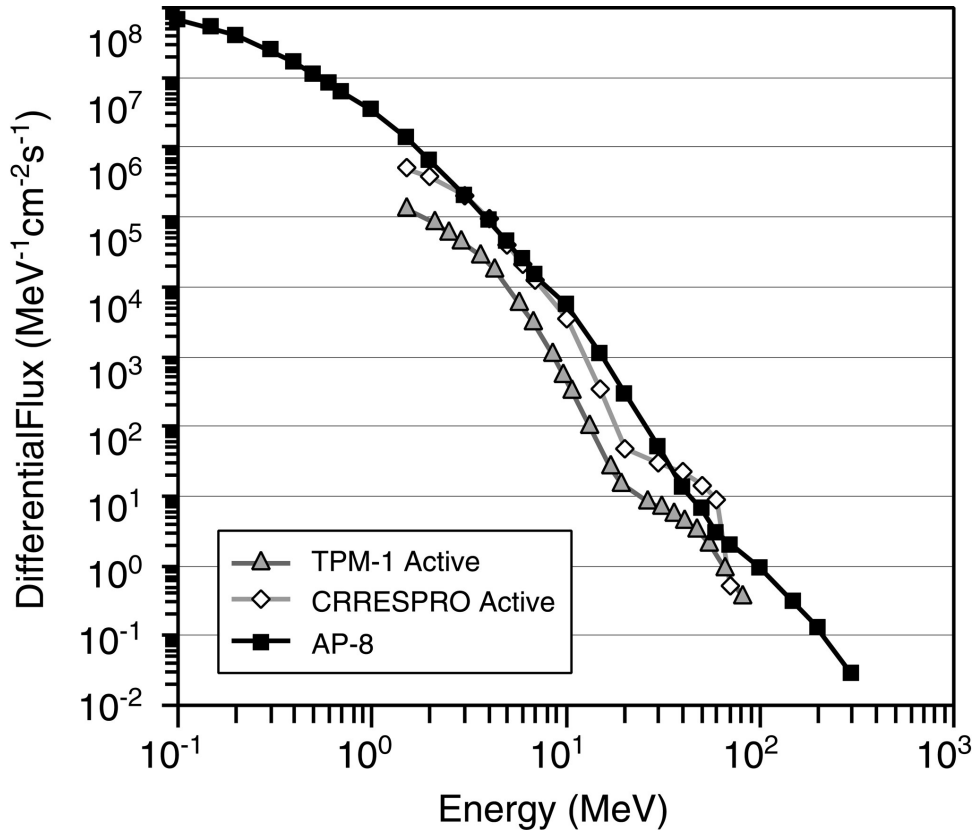


Figure 16. Comparison of trapped proton models for an elliptical orbit during active conditions and the solar maximum time period [La05].

E. Characteristics of Trapped Electrons

Some of the characteristics of trapped electrons are summarized in Table 2. There is both an inner and an outer zone or belt of trapped electrons. These two zones are very different so the characteristics are listed separately. The inner zone ranges out to an L -value of about 2.8. The electron energies range up to approximately 4.5 MeV. The flux reaches a peak near $L = 1.5$ and the value is about $10^6 \text{ cm}^{-2}\text{s}^{-1}$ for > 1 MeV electrons. These fluxes gradually increase during solar maximum by a factor of 2 to 3. This electron population, though, tends to remain relatively stable. The outer zone has L -values ranging between about 2.8 and 10. The electron energies are generally less than approximately 10 MeV. Here the region of peak flux is between L -values of 4.0 and 4.5 and the long-term average value for > 1 MeV electrons is roughly $3 \times 10^6 \text{ cm}^{-2}\text{s}^{-1}$. This zone is very dynamic and the fluxes can vary by orders of magnitude from day to day.

The distribution of trapped particles is a continuous one throughout the inner and outer zones. However, between the two high intensity zones is a region where the fluxes are at a local minimum during quiet periods. This is known as the slot region. The exact location and extent of the slot region depends on electron energy but it is between L -values of 2 and 3. The slot region is an attractive one for certain types of missions due to the increased spatial coverage compared to missions in LEO. However, the radiation environment of this region is very dynamic.

Trapped electrons contribute to TID effects, displacement damage effects and charging/discharging effects. As discussed previously, the metric for describing TID effects is dose. In a fashion analogous to protons, the metric for electron-induced displacement damage is either 1 MeV equivalent electron fluences or displacement damage dose. It should be noted though that the application of the displacement damage dose concept is not as straight forward for electrons as it is for protons [Wa04]. Finally, charging/discharging effects can be either spacecraft surface charging caused primarily by low energy electrons or deep dielectric charging caused by high energy electrons. A key parameter for these analyses is the potential difference induced by charging between a dielectric and a conductive surface.

Table 2. Trapped Electron Characteristics.

	<i>L</i> -Shell Values	Energies	Fluxes* (> 1 MeV)
Inner Zone	1 to 2.8	Up to 4.5 MeV	$10^6 \text{ cm}^{-2}\text{s}^{-1}$
Outer Zone	2.8 to 10	Up to 10 MeV	$3 \times 10^6 \text{ cm}^{-2}\text{s}^{-1}$

* long-term average

F. The AE-8 Model

The long-time standard model for trapped electrons has been the AE-8 model [Ve91], [Ve91a], [Ba97]. It consists of two static flux maps of trapped electrons – one for solar maximum and one for solar minimum conditions. Due to the variability of the outer zone electron population, the AE-8 model is valid only for long periods of time. Fig. 17 is a contour plot of the trapped electron population with energies > 1 MeV shown in dipole coordinates. The structure of the inner and outer zones is clearly seen. Since AE-8 is based on an internal magnetic field model, results are shown only out to geosynchronous altitudes but the trapped electron population exists well beyond this. An interesting feature of the outer belt is that it extends down to low altitudes at high latitudes.

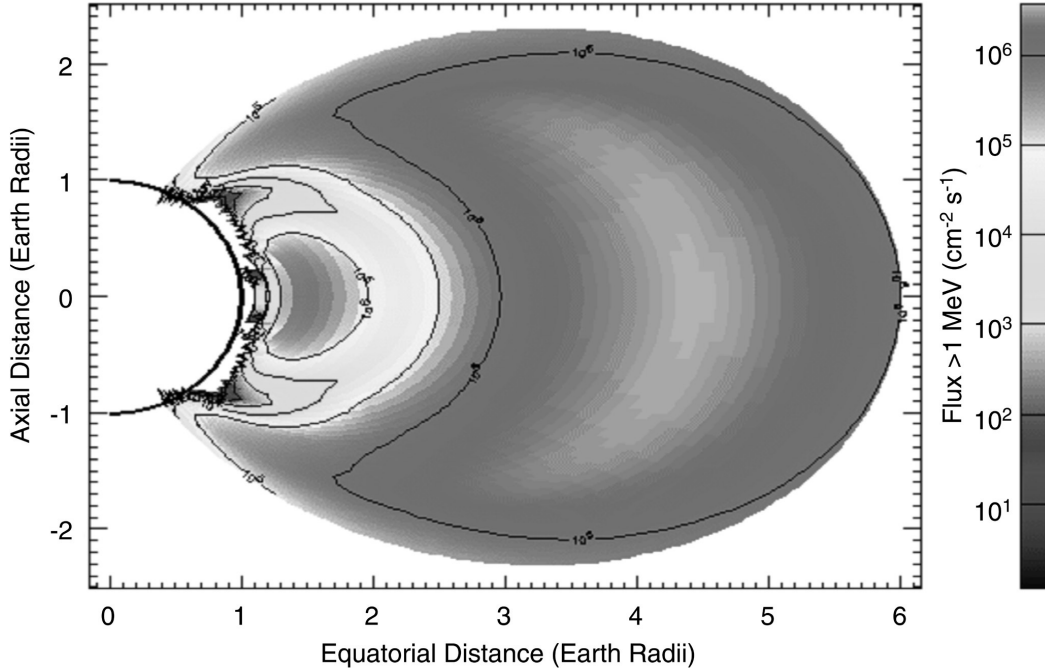


Figure 17. The electron population with energies > 1 MeV as predicted by the AE-8 model for solar maximum conditions. From SPENVIS, [http].

G. Recent Developments in Trapped Electron Models

If only the trapped particle populations are considered, the inner zone is often dominated by radiation effects due to trapped protons while the outer zone is often dominated by radiation effects due to trapped electrons. Thus, recent trapped electron models have focused on the outer zone. A feature of the outer zone is its high degree of variability and dynamic behavior. This results from geomagnetic storms and substorms, which cause major perturbations of the geomagnetic field. For example, processes such as coronal mass ejections and solar flares cause disturbances in the solar wind, which subsequently interacts with the earth's magnetosphere. Energy is extracted from the solar wind, stored and dissipated, resulting in the injection and redistribution of electrons into the magnetosphere. Although the physical details of the injection mechanisms are not completely understood, recent measurements from the Upper Atmosphere Research Satellite (UARS) illustrate the high degree of variability of electron flux levels prior to and after such storms. Figure 18 shows the electron energy spectra for $3.25 < L \leq 3.5$ after long-term decay from a prior storm (day 235) and two days after a large storm (day 244) compared to the average flux level over a 1000 day period [Pe01]. It is seen for example, at 1 MeV, that the difference in the one-day averaged differential fluxes over a 9-day period is about 3 orders of magnitude.

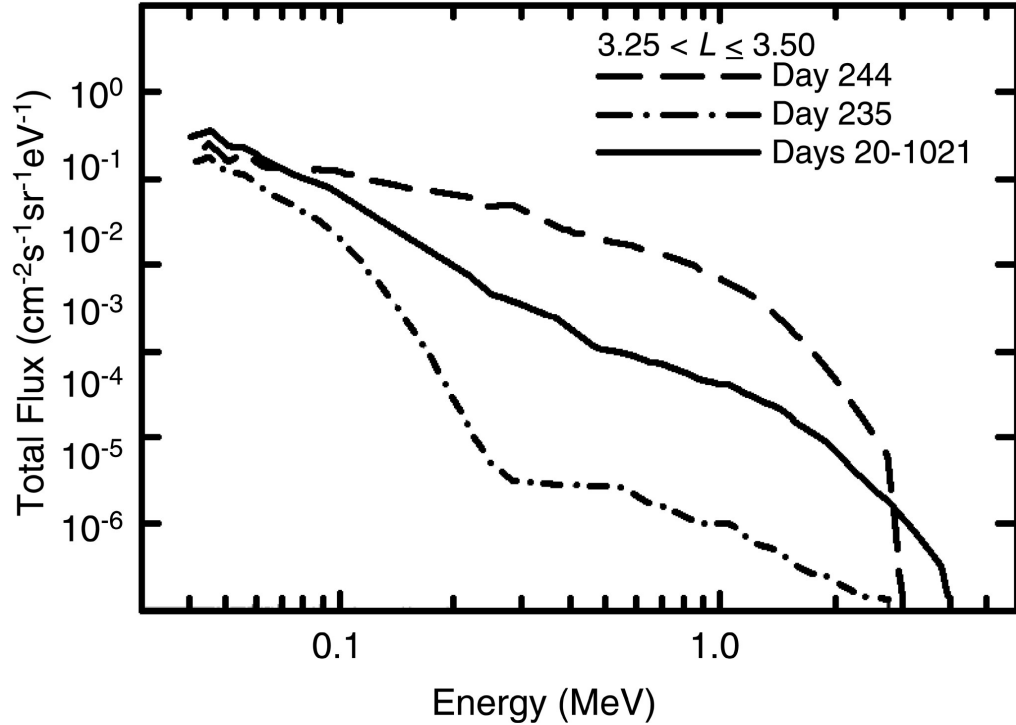


Figure 18. Total electron flux before and after a geomagnetic storm compared to a long-term average as measured onboard the UARS [Pe01].

Due to the volatile nature of the outer zone, it seems reasonable to resort to probabilistic methods in order to improve on the AE-8 model. The average flux measured during a period of time will approach the long-term average as the measurement period increases. This is illustrated in Figure 19, which is a statistical model of the median, 10th and 90th percentile fluxes measured in geostationary orbit by instrumentation onboard METEOSAT-3 [Da96]. The abscissa is the time period of the measurement and ranges from about one day to a little over one year. This figure indicates that about a month of data in the 200 to 300 keV energy range must be accumulated in this orbit in order to approximate the median flux. It turns out that even longer periods are needed for higher energy electrons and for orbits with lower L -values. These type calculations can also be used to put a constraint on the period of time over which a long-term model such as AE-8 should be used. A conservative rule of thumb is that AE-8 should not be applied to a period any shorter than 6 months. A model such as that shown in Fig. 19 is also useful for estimating worst-case fluxes averaged over different time scales.

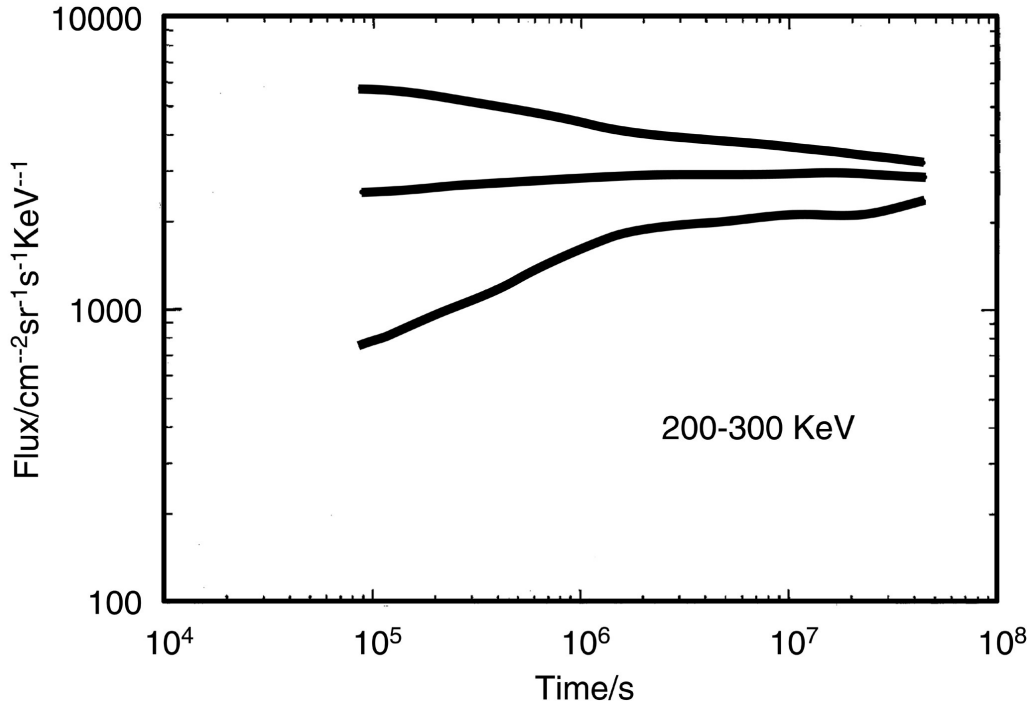


Figure 19. Statistical model of the median, 10th and 90th percentile fluxes in geostationary orbit for approximately 200 to 300 keV electrons [Da96].

Instrumentation onboard UARS was used to construct a probabilistic model during the declining phase of solar cycle 22 [Pe01]. Figure 20 shows the probability of encountering a daily- averaged, > 1 MeV trapped electron flux for a given L -value. Note that such a probability plot indicates both the most frequently occurring flux value and its variation for a given L . The values of L covered in this work range from about 2 to 7. Note that for L -shells between 2 and 3 corresponding to the slot region, the highest probabilities correspond to the lowest observed fluxes. However, the overall range of possible flux values is several orders of magnitude, indicating the volatility of the region. Figure 20 shows the highest fluxes are between L -values of 3.5 and 4.5. For $L > 4.5$ the fluxes decrease steadily with increasing L .

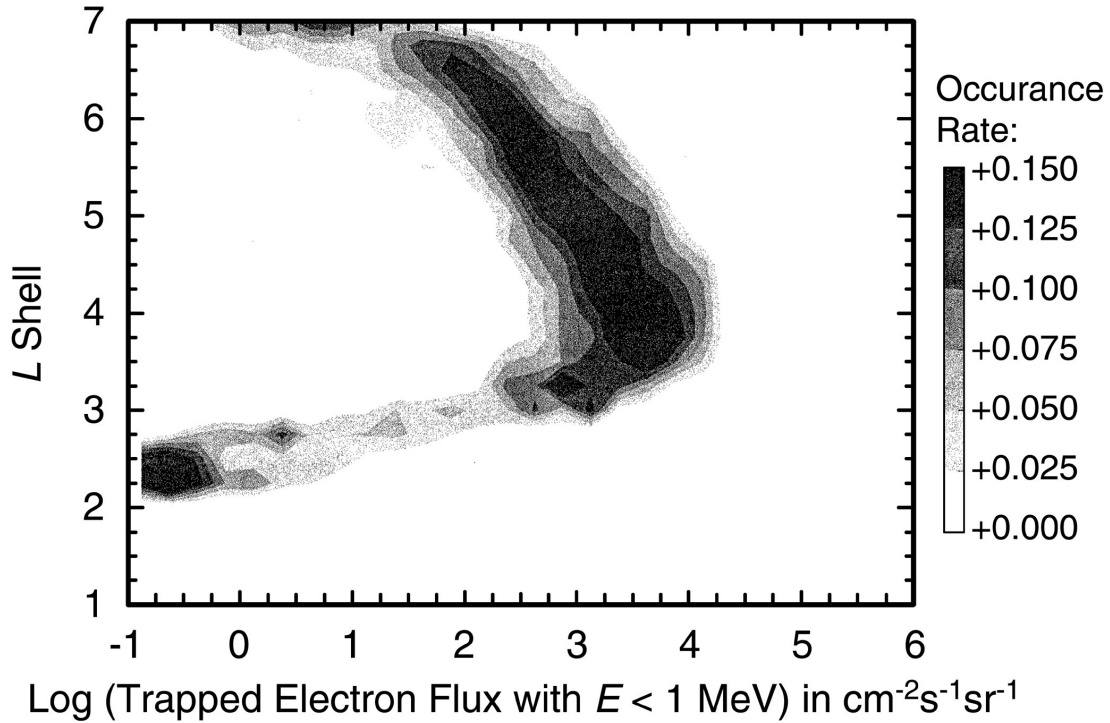


Figure 20. Probability plot of encountering a given > 1 MeV electron flux at a given L -value during the declining phase of solar cycle 22 [Pe01].

The observations made of the slot region with instrumentation onboard the UARS satellite are consistent with recent results obtained from the TSX5 mission over an approximately 4 year period [Br04]. Figure 21 shows a cumulative probability plot of daily averaged > 1.2 MeV electron fluxes in this region. The distribution shows the probability that a daily averaged flux exceeds the threshold flux shown on the x-axis. The well-known “Halloween-2003” storm occurred during this mission and is shown for reference along with results for the AE-8 model. Interestingly, these measurements show that the AE-8 model results were exceeded every day during the 4-year mission.

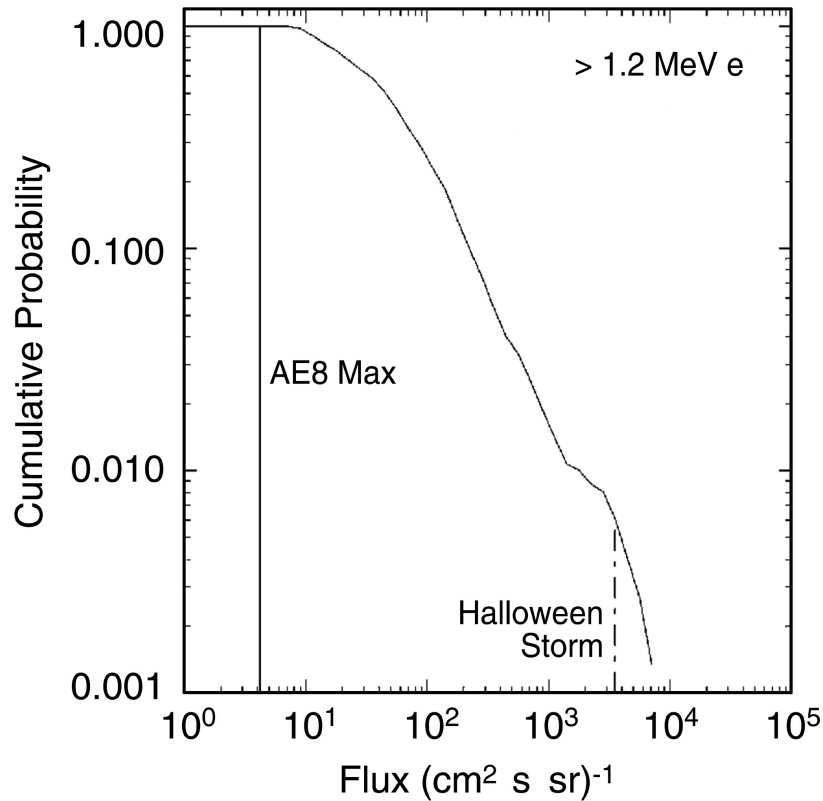


Figure 21. Cumulative probability plot of > 1.2 MeV electron fluxes observed in the slot region during the 4-year TSX5 mission [Br04].

The statistical models discussed above give results for both an average flux and some indicator of the dispersion that can be used for determining a worst-case flux. Probabilistic approaches exist that focus only on worst-case scenarios. One such method is that of extreme value statistics. Extreme value methods are discussed in section VB4. These methods have been used to study daily-averaged fluxes of > 2 MeV electrons measured by the GOES satellites. It has been estimated from about one solar cycle of data that the largest observed flux on March 28, 1991 ($8 \times 10^4 \text{ cm}^{-2}\text{s}^{-1}\text{sr}^{-1}$) would be exceeded once every 20 years [Ko01]. Although this result in itself is of minimal use for radiation effects applications, the overall utility of such an approach for analyzing trapped electron flux variations is relatively unexplored.

The FLUX Model for Internal Charging (FLUMIC) [Wr00] software tool was developed as a worst-case daily flux model of the outer belt to be used with the deep dielectric charging model DICTAT. The model is based on data from several satellites in the > 0.2 to > 5.9 MeV range taken between 1987 and 1998. It uses fits to the most intense electron enhancements over this time period to account for properties such as energy spectra and solar cycle and seasonal dependence. The result is a model of the highest fluxes of penetrating electrons expected during a mission.

Another general approach to describe the trapped electron fluxes in the outer belt is to relate them to the level of disturbance of the geomagnetic field. There are several geomagnetic indices that could possibly be used as a basis for this. Brautigam, Gussenhoven and Mullen developed a quasi-static model of outer zone electrons ordered by a 15-day running average of the geomagnetic activity index, A_p [Br92]. The A_p index is an indicator of the general level of

global geomagnetic disturbance. The daily outer zone electron energy spectra during the CRRES mission were separated according to the Ap index and averaged, thus producing flux profiles based on geomagnetic activity. The result is the basis for the CRRESELE model. An example of this is shown in Fig. 22 for 0.95 MeV differential electron fluxes for 6 levels of geomagnetic activity [Gu96]. It is seen that the flux changes are much larger for the smaller *L*-shell values shown. The current CRESSELE model, which is valid for solar maximum, features flux profiles ranging for 6 levels of geomagnetic activity, an average profile, and a worst-case profile encountered during the mission.

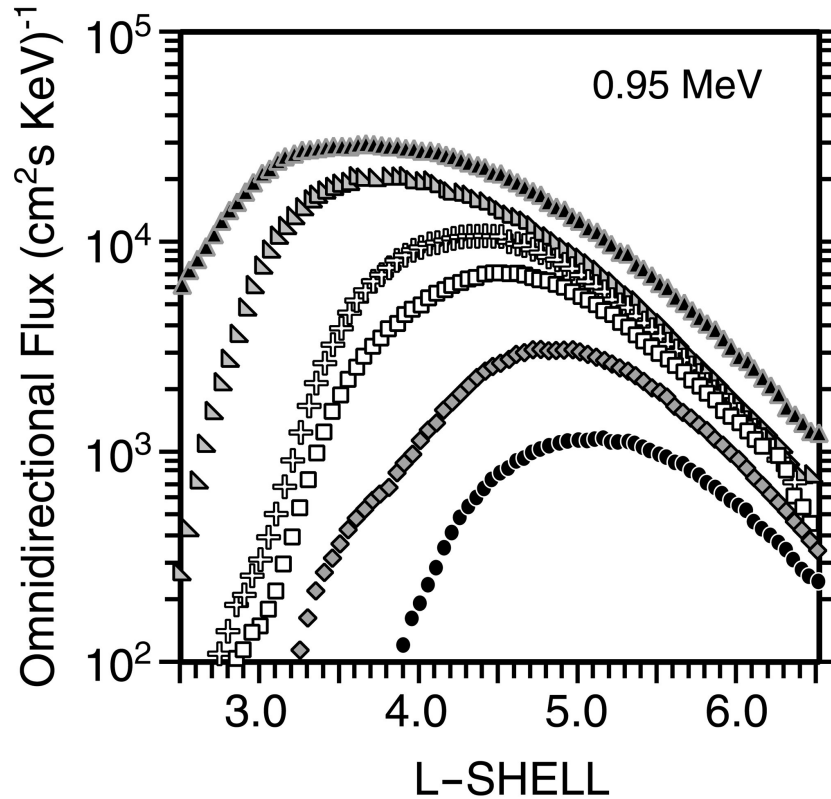


Figure 22. Differential electron energy spectra centered at 0.95 MeV during the CRRES mission for 6 different 15-day running average values of the Ap geomagnetic index. As conditions become more disturbed, the fluxes increase [Gu96].

Spurred on by the CRRESELE model, the European Space Agency funded an effort to further develop models of outer zone electrons based on geomagnetic activity indices [Va96]. The CRRES data were used to train neural networks using the geomagnetic index Kp as input. This is another general indicator of the global geomagnetic disturbance, similar to the Ap index. Thirty networks were trained to estimate flux intensities at 5 energies and 6 *L*-values during the CRRES time period. A simulated data base of electron flux intensities was subsequently generated dating back to 1932 when the Kp index was first tracked. The validity of using 14 months of data to generate a simulated catalog of 60+ years of fluxes in this manner is unknown. The goal of this effort was to use the simulated fluxes to develop improved models. Currently

there exists the ESA-SEE1 model that was developed from this effort. It represents an average flux map of trapped electrons during solar minimum and was intended as a replacement for AE-8 during this time period.

The initial version of the Particle ONERA-LANL Environment (POLE) model for the geostationary electron environment was developed in 2003 [Bo03]. It is based on 25 years (1976-2001) of Los Alamos satellite data and is the most detailed model available of trapped electron data over the course of a solar cycle. It provides mean, worst-case and best-case fluxes with a time resolution of one year. The initial model covered the energy range of 30 keV to 2.5 MeV. A recent update has extended the upper energy range to 5.2 MeV and added 3 more years worth of data [Si06]. Figure 23 shows the evolution of the mean electron flux over about 2.5 solar cycles for the complete electron energy range of the satellite data. It is seen that the lower energies show relatively little variation with time while the higher energies tend to reach their maximum flux during the declining phase of the solar cycle.

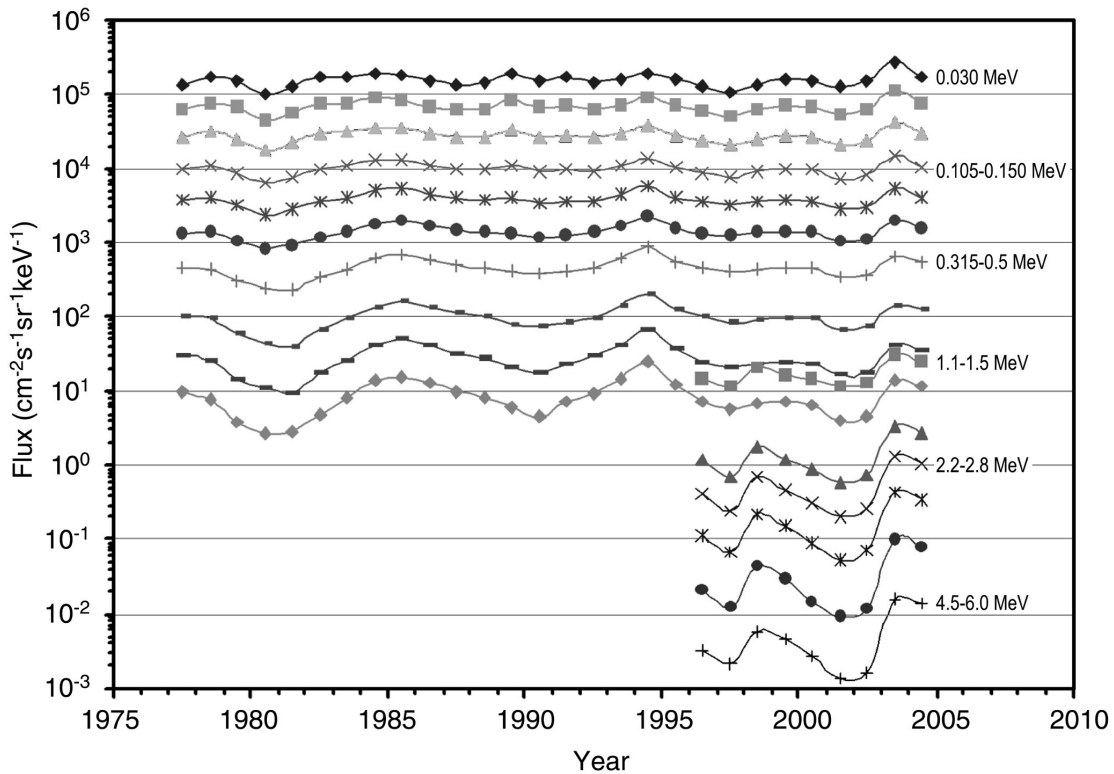


Figure 23. Time and energy dependence of the mean electron flux at geostationary altitudes over about 2.5 solar cycles [Si06].

It is interesting to see how these more recent models compare with the traditional AE-8 model for common orbits. Keep in mind that AE-8 is supposed to represent the average flux for the period and orbit of interest. Figure 24 is a comparison of the average electron fluxes as a function of energy for POLE, CRRESELE and AE-8 predictions for a geostationary orbit. Figure 25 is a similar comparison except that worst-case predictions are presented. Results for the FLUMIC model, a worst-case model, are also shown in Figure 25. It is seen that generally,

the predicted fluxes for AE-8 are rather high compared to the average fluxes predicted by the other models except at the very lowest and very highest energies. For the worst case predictions in Figure 25, there is a rather large spread in the results at low energies, but the predictions converge for energies beyond about 1 MeV.

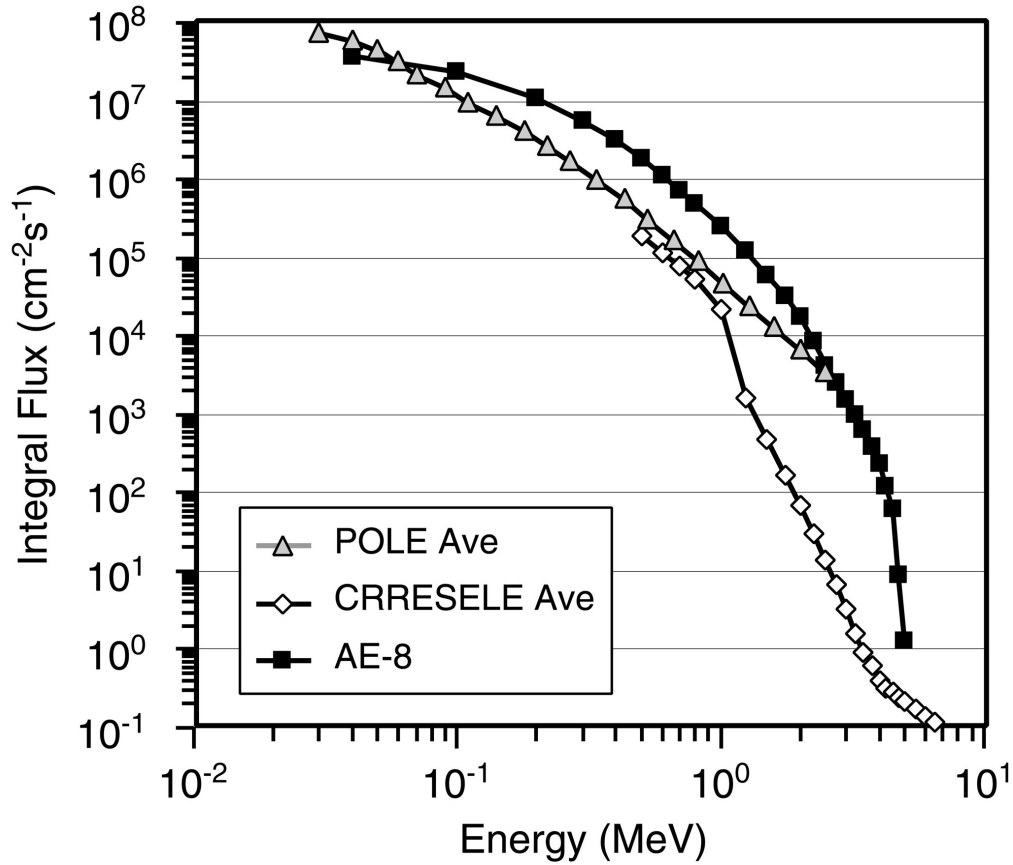


Figure 24. Model comparisons for average electron fluxes of POLE and CRRESELE at geostationary altitudes to AE-8 [La05].

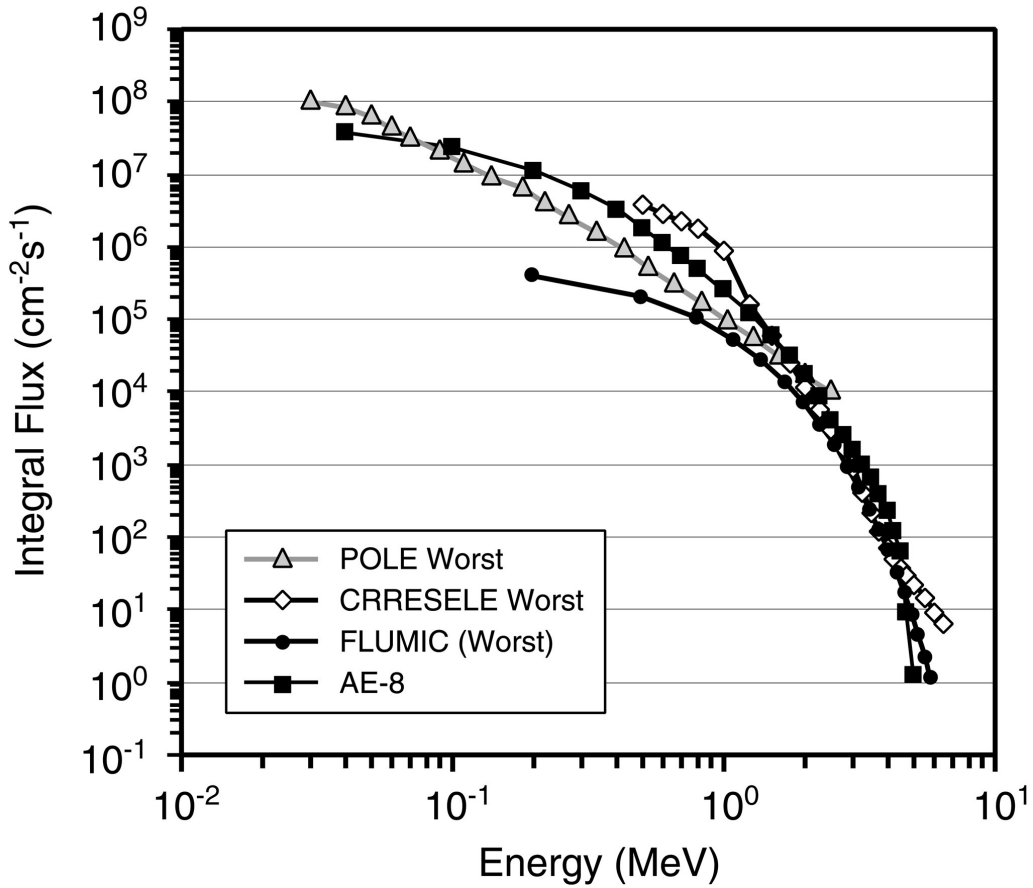


Figure 25. Model comparisons for worst case electron fluxes of POLE, CRRESELE and FLUMIC at geostationary altitudes to AE-8 [La05].

Finally, Fig. 26 compares the POLE model at solar maximum and solar minimum with AE-8 for a geostationary orbit. There is no distinction between these two periods in the AE-8 model at geostationary altitudes. The POLE model shows little difference between solar maximum and solar minimum at low energies but shows higher fluxes during solar minimum at higher energies.

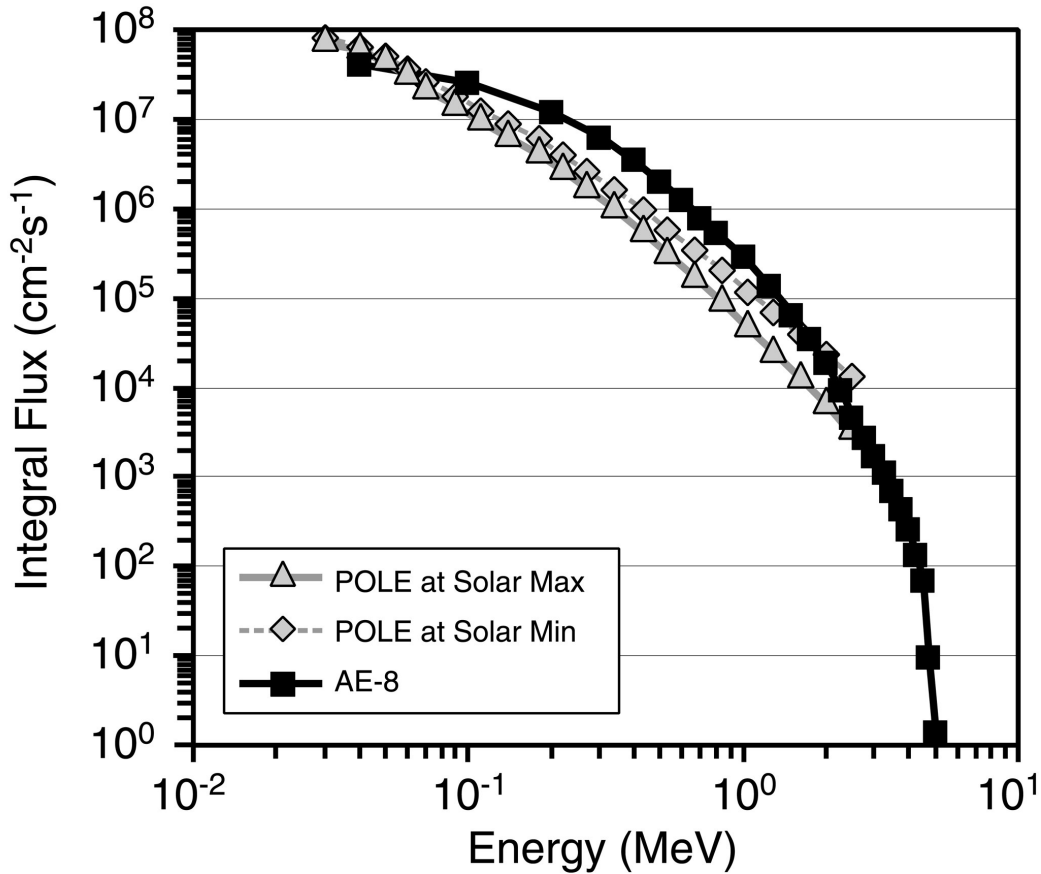


Figure 26. Comparison of the POLE model to AE-8 at geostationary altitudes for solar maximum and solar minimum conditions [La05].

It is seen that in geostationary orbit, the predictions of AE-8 are generally higher than the average flux predictions of more recent models. In fact, AE-8 is more similar to some of the worst-case flux models than the average flux models. Other comparisons for elliptical MEO are shown in Lauenstein, [La05].

IV. Galactic Cosmic Rays

A. General Characteristics

Galactic cosmic rays (GCR) are high-energy charged particles that originate outside of our solar system and are believed to be remnants from supernova explosions. Some general characteristics are listed in Table 3. They are composed mainly of hadrons, the abundances of which is listed in the Table. A more detailed look at the relative abundances is shown in Figure 27. All naturally occurring elements in the Periodic Table (up through uranium) are present in GCR, although there is a steep drop-off for atomic numbers higher than iron ($Z=26$). Energies can be as high as 10^{11} GeV, although the acceleration mechanisms to reach such high energies are not understood. Fluxes are generally a few $\text{cm}^{-2}\text{s}^{-1}$, and vary with the solar cycle. Typical

GCR energy spectra for a few of the major elements during solar maximum and solar minimum are shown in Figure 28. It is seen the spectra tend to peak around 1 GeV per nucleon. The flux of the ions with energies less than about 10 GeV per nucleon is modulated by the magnetic field in the sun and solar wind. During the high activity solar maximum period there is significantly more attenuation of the flux, resulting in the spectral shapes shown in Figure 28.

Table 3. Characteristics of Galactic Cosmic Rays.

Hadron Composition	Energies	Flux	Radiation Effects	Metric
87% protons 12% alphas 1% heavier ions	Up to 10^{11} GeV	1 to $10 \text{ cm}^{-2}\text{s}^{-1}$	SEE	LET

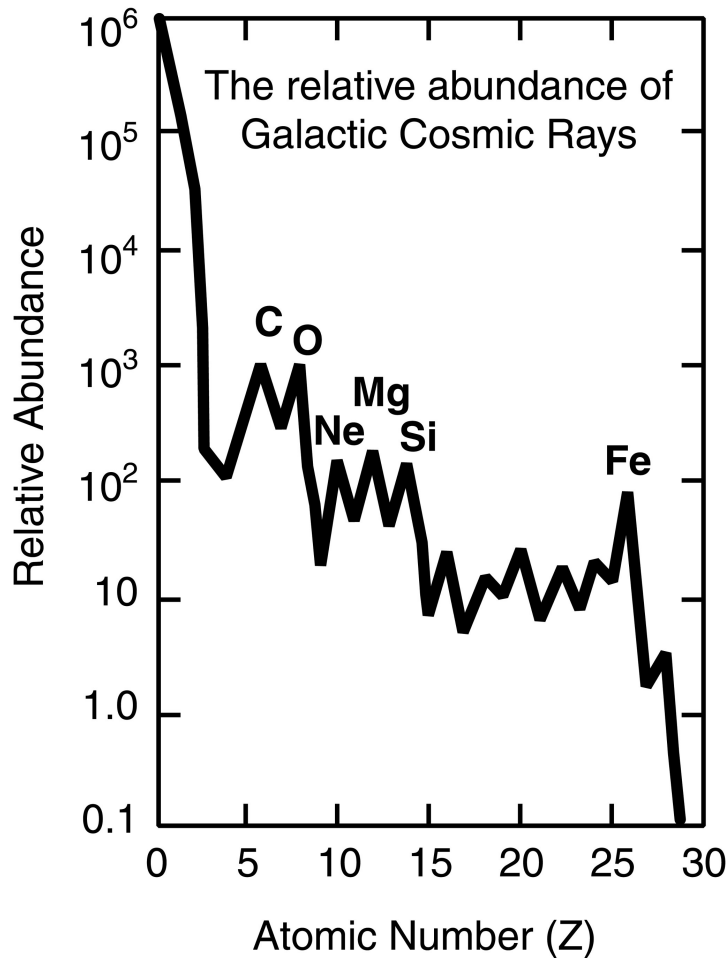


Figure 27. Abundances of GCR up through Z = 28.

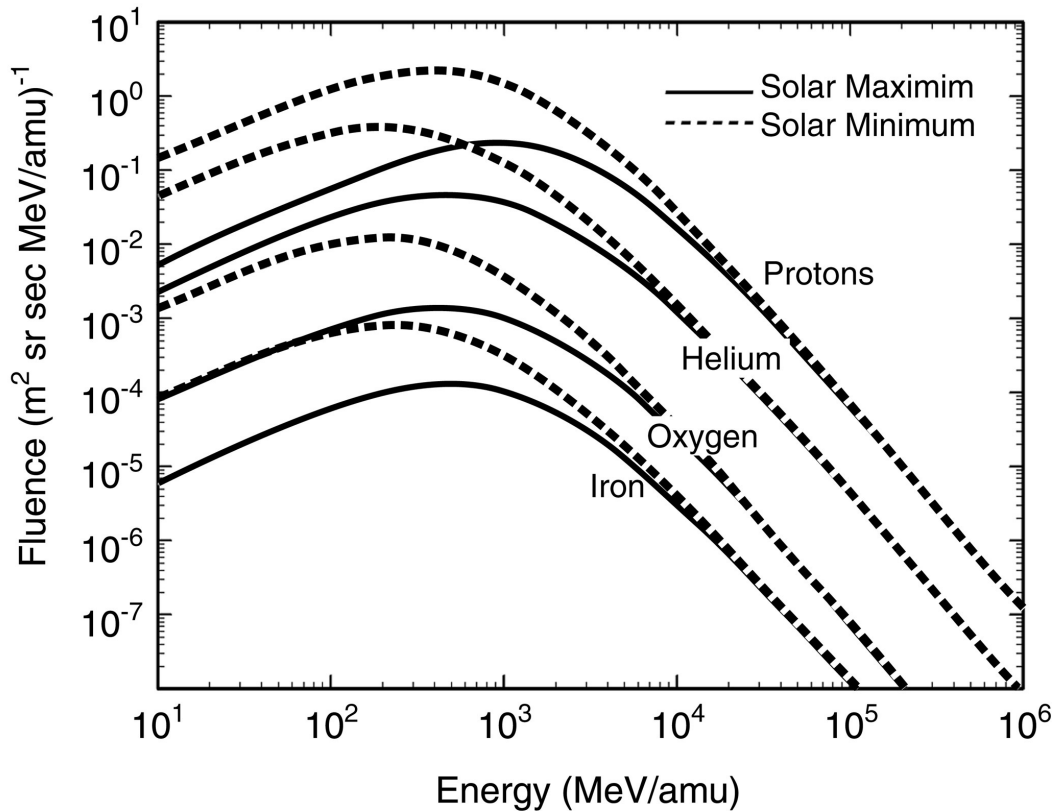


Figure 28. GCR energy spectra for protons, helium, oxygen and iron during solar maximum and solar minimum conditions [Ba96a].

SEE are the main radiation effects caused by GCR in microelectronics and photonics. The metric traditionally used to describe heavy ion induced SEE is linear energy transfer (LET). LET is the energy lost by the ionizing particle per unit path length in the sensitive volume. For SEE studies the path length is often divided by the material density and expressed as an areal density. The units of LET that are commonly used are then $\text{MeV}\cdot\text{cm}^2/\text{mg}$.

For SEE analyses energy spectra such as those shown in Figure 28 are often converted to LET spectra. Such integral LET spectra for solar maximum and solar minimum conditions are shown in Figure 29. These spectra include all elements from protons up through uranium. The ordinate gives the flux of particles that have an LET greater than the corresponding value shown on the abscissa. Given the dimensions of the sensitive volume this allows the flux of particles that deposit a given amount of charge or greater to be calculated in a simple approximation.

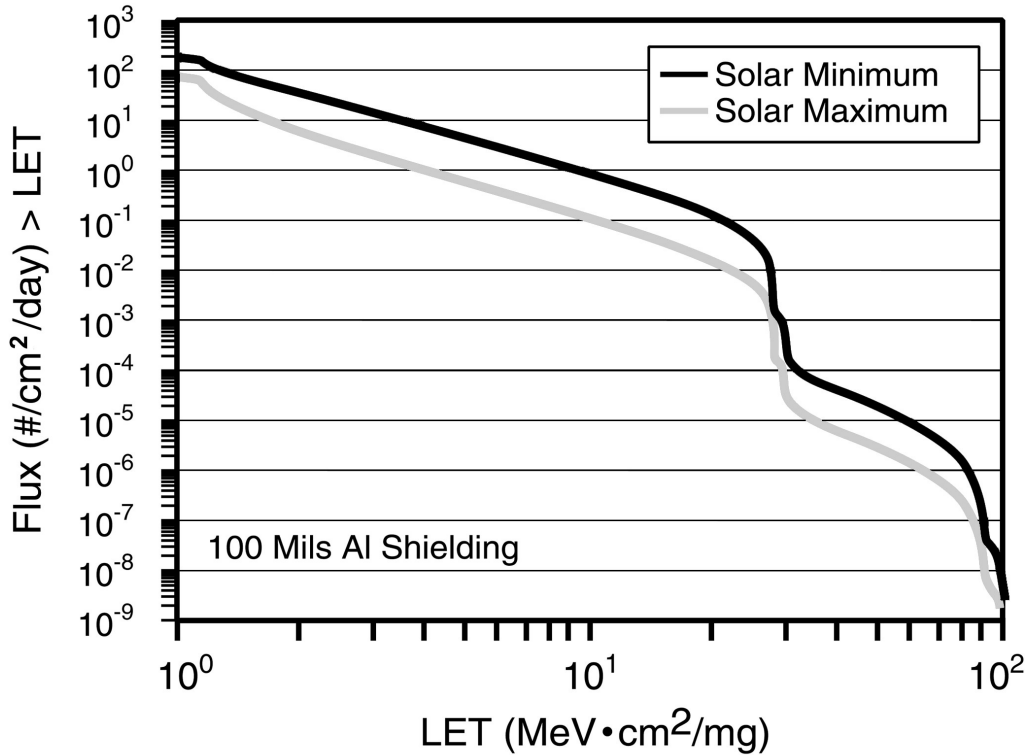


Figure 29. Integral LET spectra for GCR during solar maximum and solar minimum.

The LET spectra shown in Figure 29 are applicable to geosynchronous and interplanetary missions where there is no geomagnetic attenuation. The earth's magnetic field, however, provides significant protection. Due to the basic interaction of charged particles with a magnetic field, the charged particles tend to follow the geomagnetic field lines. Near the equator the field lines tend to be parallel to the earth's surface. Thus all but the most energetic ions are deflected away. In the polar regions the field lines tend to point toward the earth's surface, which allows much deeper penetration of the incident ions. The effect of the geomagnetic field on the incident GCR LET spectrum during solar minimum is discussed for various orbits in [Ba97].

B. Galactic Cosmic Ray Models

The original Cosmic Ray Effects in MicroElectronics (CREME) suite of programs of Adams [Ad87] was developed specifically for microelectronics applications. It turned out to be a very useful and popular tool and has been updated since then. CREME96 is the most recent version [Ty97] and uses the GCR model of Moscow State University (MSU) [Ny96a].

In principle the MSU model is similar in approach to a GCR model that was originated independently at NASA by Badhwar and O'Neill [Ba96a]. Both models are based on the diffusion-convection theory of solar modulation [Pa85]. This is used to describe the penetration of cosmic rays into the heliosphere from outside and their transport to near earth at 1 Astronomical Unit (AU). The solar modulation is used as a basis to describe the variation of GCR energy spectra over the solar cycle, as shown in Figure 28. However, the implementation of the solar modulation theory for the two models is different. The Badhwar and O'Neill model

estimates the modulation level from GCR measurements at 1 AU. Correlations to ground-based neutron monitor counting rates are then made to establish long-term predictive capability. The MSU model is not as direct but uses multi-parameter fits to ultimately relate solar cycle variations in GCR intensity to observed sunspot numbers.

Comparisons of the GCR proton and alpha particle spectra of the two models above plus that used in the QinetiQ Atmospheric Radiation Model (QARM) show discrepancies among all three models for narrow time ranges [Le06]. Examples of this are shown in Figure 30 for protons. This is not surprising considering the details of the solar modulation implementation are different. However, similar predictions are seen for the total fluence over the course of a solar cycle.

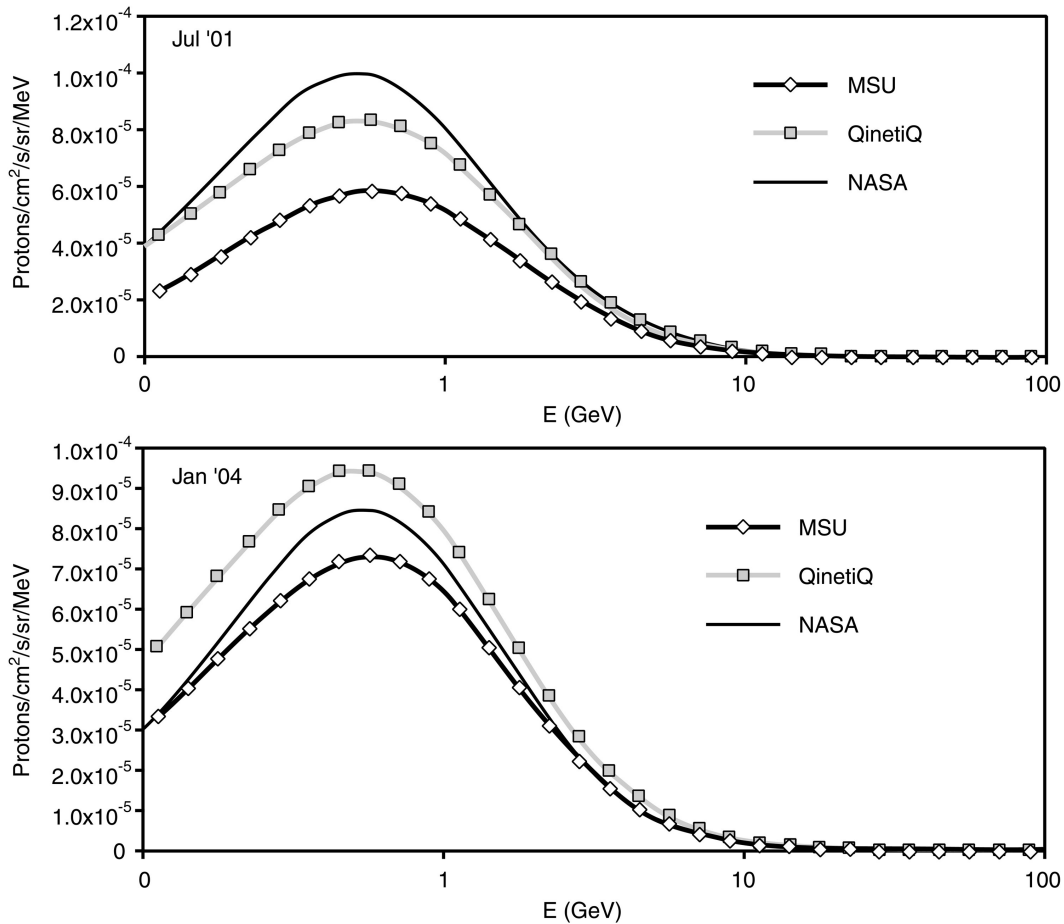


Figure 30. GCR proton energy spectra predicted by the MSU, Badhwar and O'Neill, and QARM models for two different dates [Le06].

The recent high-quality measurements of GCR heavy ion energy spectra taken on the ACE satellite make possible a stringent test of the GCR models. Comparisons of model results and the ACE data for the 1997 solar minimum period are shown in Figure 31 for 4 of the major elements in the energy range of about 50 to a few hundred MeV per nucleon. It is seen that both models yield good results for heavy ions. Over the range of data shown, the NASA model of

Badhwar and O'Neill tends to have a more accurate spectral shape while the MSU model tends to show a smaller root-mean-square deviation from the data.

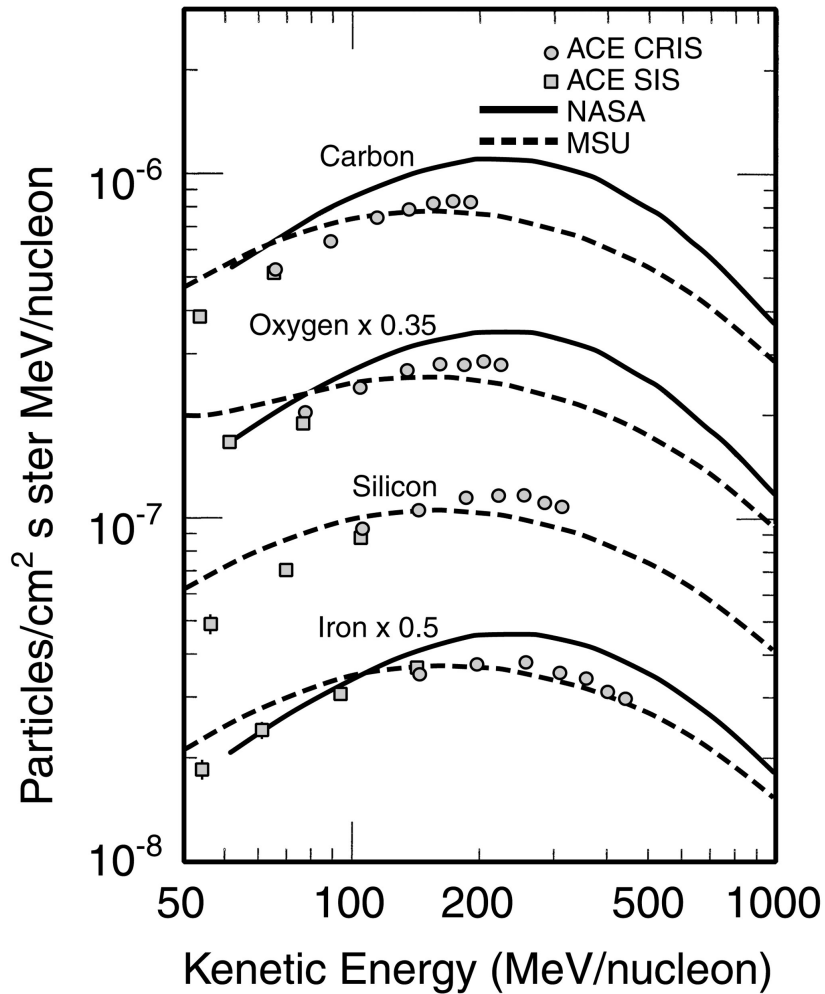


Figure 31. Comparison of the NASA model of Badhwar and O'Neill and the MSU model to measurements made with instrumentation onboard the ACE satellite during 1997 [Da01].

A recent development led by the California Institute of Technology is to use a transport model of GCR through the galaxy preceding the penetration and subsequent transport in the heliosphere. [Da01]. During the initial propagation of GCR through the galaxy use is made of knowledge of astrophysical processes that determine the composition and energy spectra of GCR. Comparisons of the fitted model spectra to the ACE satellite measurements are shown in Figure 32. The elements C and Fe are GCR primaries while B, Sc, Ti and V are GCR secondaries produced by fragmentation of primaries on interstellar H and He. The goal of this new approach is to provide an improved description of GCR composition and energy spectra throughout the solar cycle.

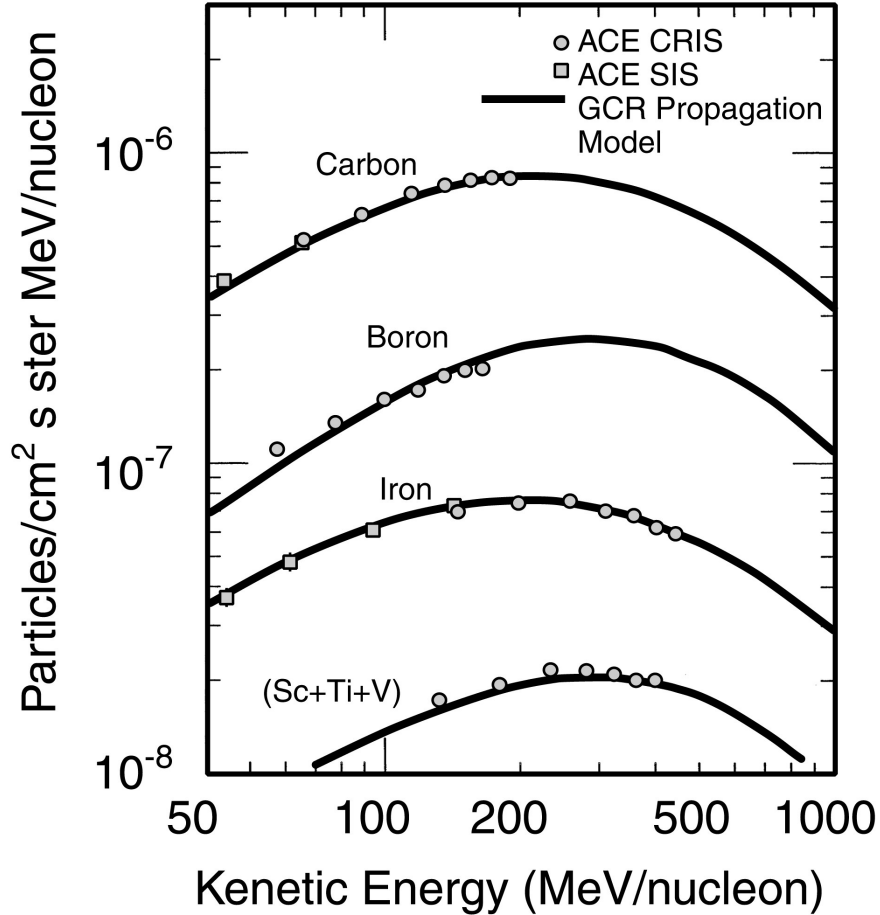


Figure 32. The new approach of the California Institute of Technology to describe GCR energy spectra compared to the ACE data during 1997 [Da01].

V. Solar Particle Events

A. General Characteristics

It is believed that there are 2 categories of solar particle events and that each one accelerates particles in a distinct manner. Solar flares result when the localized energy storage in the coronal magnetic field becomes too great and causes a burst of energy to be released. They tend to be electron rich, last for hours, and have an unusually high ^3He content relative to ^4He . A Coronal Mass Ejection (CME), on the other hand, is a large eruption of plasma (a gas of free ions and electrons) that drives a shock wave outward and accelerates particles. CMEs tend to be proton rich, last for days, and have a small ^3He content relative to ^4He . A review article by Reames gives a detailed account of the many observed differences between solar flares and CMEs [Re99].

CMEs are the type of solar particle events that are responsible for the major disturbances in interplanetary space and the major geomagnetic disturbances at earth when they impact the magnetosphere. The total mass of ejected plasma in a CME is generally around 10^{15} to 10^{17} grams. Its speeds can vary from about 50 to 1200 km/s with an average speed of around 400

km/s. It can take anywhere from about 12 hours to a few days to reach the earth. Table 4 lists some further general characteristics of CMEs.

Table 4. Characteristics of CMEs.

Hadron Composition	Energies	Integral Fluence (>10MeV/nucleon)	Peak Flux (>10MeV/nucleon)	Radiation Effects
96.4% protons 3.5% alphas ~0.1% heavier ions	Up to ~GeV/nucleon	$>10^9 \text{ cm}^{-2}$	$>10^5 \text{ cm}^{-2}\text{s}^{-1}$	TID DD SEE

All naturally occurring chemical elements ranging from protons to uranium are present in solar particle events. They can cause permanent damage such as TID and DD that is due mainly to the proton and possibly alpha component. Just because the heavy ion content is a small percentage does not mean it can be ignored. Heavy ions, as well as protons and alpha particles in solar particle events, can cause both transient and permanent SEE.

Figures 33 and 34 illustrate the periodic yet statistical nature of solar particle events. They are plots of the daily solar proton fluences measured by the IMP-8 and GOES series of spacecraft over an approximately 28 year period. Figure 33 shows > 0.88 MeV fluences while Figure 34 shows > 92.5 MeV fluences. The solar maximum and solar minimum time periods are shown in the figures to illustrate the dependence on solar cycle for both low energy and high-energy protons.

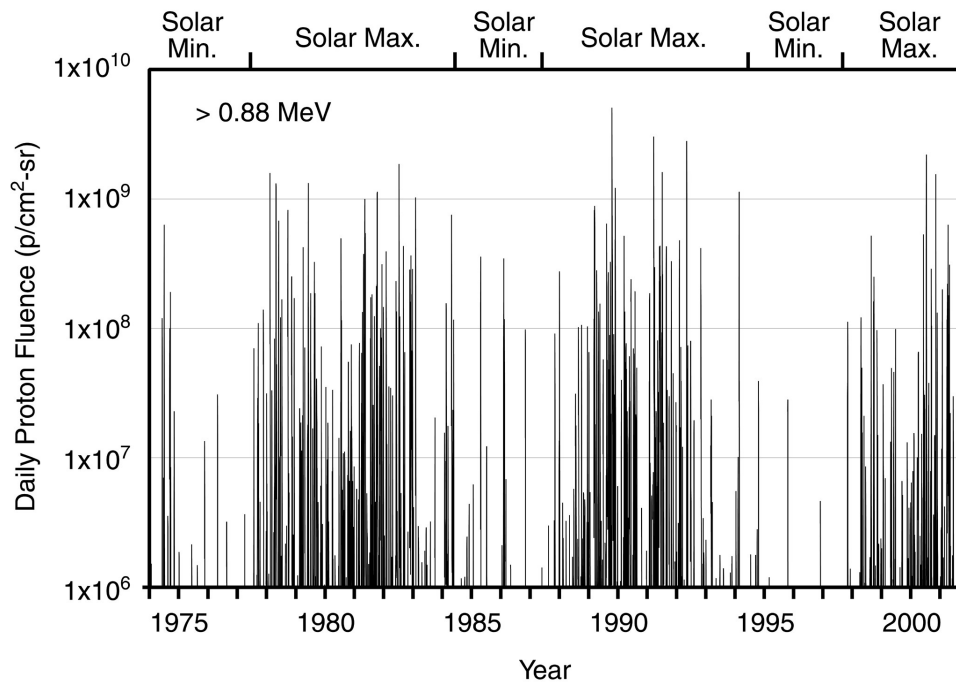


Figure 33. Daily fluences of > 0.88 MeV protons due to solar particle events between approximately 1974 and 2002.

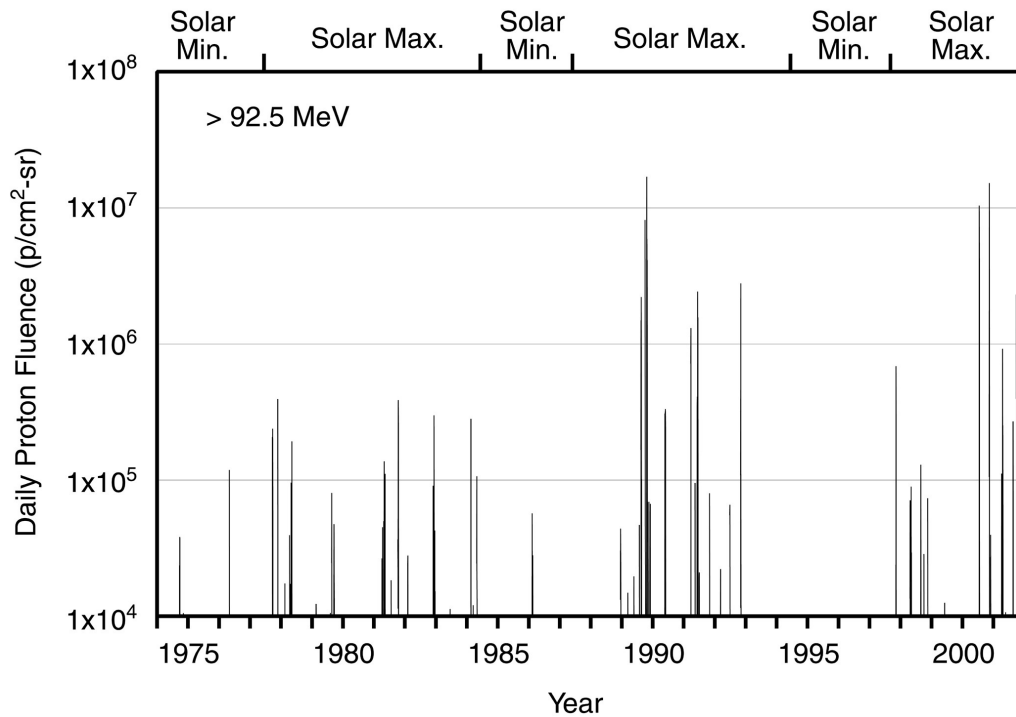


Figure 34. Daily fluences of > 92.5 MeV protons due to solar particle events between approximately 1974 and 2002.

The available solar particle data that cover the largest period of time are for protons. Since the available solar heavy ion data are not nearly as extensive, solar proton models and solar heavy ion models will be discussed separately.

B. Solar Proton Models

Sections B1 – B5 describe the application of probabilistic models to solar proton event data, including the origin of the models. This will be done in a sequence that emphasizes the construction of a set of tools that are useful to the design engineer starting from the basics. Section B1 describes the distribution of event magnitudes. B2 and B3 describe modeling cumulative fluences over the course of a mission. B4 discusses worst-case events during a mission. Finally, B5 describes a model that has implications for the energy release and predictability of events. It indicates a potential new direction toward a physically based model for solar proton events.

1. The Maximum Entropy Principle and the Distribution of Solar Proton Event Magnitudes

Given that the occurrence of solar particle events is a stochastic phenomenon, it is important to accurately model the distribution of event magnitudes. However, in general it can be rather difficult to select a probability distribution for the situation where the data are limited. There have been a number of empirical assumptions that the event magnitudes can be represented by certain distributions. For example, lognormal distributions [Ki74], [Fe91] and

power function distributions [Ga96], [Ny99] have been used. The lognormal distribution describes the large events well but underestimates the probability of smaller events. On the other hand power functions describe the smaller events well but overestimate the probability of larger events. This section describes a method for making arguably the best selection of a probability distribution for a limited set of data that is compatible with known information about the distribution.

The Maximum Entropy Principle was developed by E.T. Jaynes [Ja57] using the concept of entropy originated by Shannon [Sh49]. Jaynes showed in his studies of statistical mechanics that the usual statistical distributions of the theory could be derived by what became known as the Maximum Entropy Principle. This led Jaynes to re-interpret statistical mechanics as a form of statistical inference rather than a physical theory. It established the principle as a procedure for making an optimal selection of a probability distribution when the data are incomplete. Entropy is defined mathematically the same way as in statistical mechanics but for this purpose it is a measure of the probability distribution's uncertainty. The principle states that the distribution that should be selected is the one that maximizes the entropy subject to the constraints imposed by available information. This choice results in the least biased distribution in the face of missing information. Choosing the distribution with the greatest entropy avoids the arbitrary introduction or assumption of information that is not available. It can therefore be argued that this is the best choice that can be made using the available data.

The probability distribution's entropy, S , is defined [Ja57], [Ka89]

$$S = -\int p(M) \ln[p(M)] dM \quad (1)$$

where $p(M)$ is the probability density of the random variable M . For the case of solar particle event fluences, M is conveniently taken as the base 10 logarithm of the event fluence. A series of mathematical constraints are imposed upon the distribution, drawing from known information. In this case the constraints are [Xa99]:

- a) The distribution can be normalized.
- b) The distribution has a well-defined mean.
- c) The distribution has a known lower limit in the event fluence. This may correspond to a detection threshold, for example.
- d) The distribution is bounded and consequently infinitely large events are not possible.

The resulting system of equations are used along with equation (1) to find the solution $p(M)$ that maximizes S . This has been worked out for many situations [Ka89] and can also be solved using the LaGrange multiplier technique [Tr61]. Using this procedure the following result for solar proton event fluences has been obtained for the solar maximum time period [Xa99]:

$$N = N_{tot} \left[\frac{\phi^{-b} - \phi_{max}^{-b}}{\phi_{min}^{-b} - \phi_{max}^{-b}} \right] \quad (2)$$

where N is the number of events per solar maximum year having a fluence greater than or equal to ϕ , N_{tot} is the total number of events per solar maximum year having a fluence greater

than or equal to ϕ_{min} , $-b$ is the index of the power function, and ϕ_{max} is the maximum event fluence. Equation (2) is a truncated power function in the event fluence. It behaves like a power function with an index of $-b$ for $\phi \ll \phi_{max}$ and goes smoothly to zero at the upper limit ϕ_{max} .

Figure 35 shows > 30 MeV solar proton event data compared to the best fit to equation (2). The data are from the 21 solar maximum years during solar cycles 20 – 22. It is seen that the probability distribution derived from the maximum entropy principle describes the data quite well over its entire range. This strong agreement indicates that this probability distribution captures the essential features of a solar proton event magnitude distribution. It is a power function for small event sizes and falls off rapidly for very large events. The interpretation of the maximum fluence parameter ϕ_{max} is interesting in itself and will be discussed further in section B4.

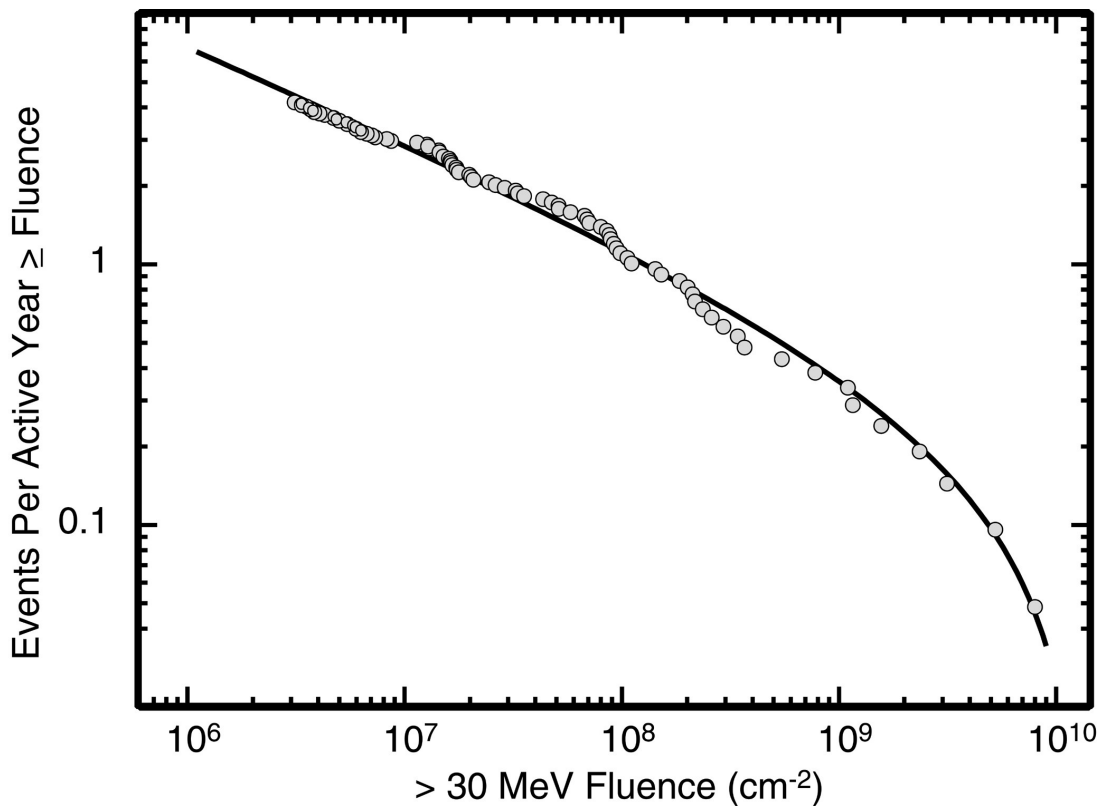


Figure 35. Comparison of the maximum entropy theory result for the distribution to 3 solar cycles of data during solar maximum [Xa99].

2. Cumulative Fluence During Solar Maximum

During a space mission the solar particle event fluence that accumulates during the solar maximum time period is often the dominant contribution to the total fluence. Thus, much prior work focuses on this period of the solar cycle. A solar cycle typically lasts about 11 years. A commonly used definition of the solar maximum period is the 7-year period that spans a starting

point 2.5 years before and an ending point 4.5 years after a time defined by the maximum sunspot number in the cycle [Fe93]. The remainder of the cycle is considered solar minimum.

Once the initial or underlying distribution of event sizes during solar maximum such as that shown in Figure 35 is known, it can be used to determine the accumulated fluence for a period of time during solar maximum. Due to the stochastic nature of the events, confidence level approaches are often used so that risk-cost-performance tradeoffs can be evaluated by the designer. The first such model was based on King's analysis of >10 to >100 MeV protons during solar cycle 20 [Ki74], [St74]. One "anomalously large" event, the well-known August 1972 event, dominated the fluence of this cycle so the model predicts the number of such events expected for a given mission length at a specified confidence level. Using additional data, a model from JPL emerged in which Feynman et al. showed that the magnitude distribution of solar proton events during solar maximum is actually a continuous distribution between small events and the extremely large August 1972 event [Fe90]. Under the assumptions that this underlying distribution can be approximated by a lognormal distribution and that the occurrence of events is a Poisson process, the JPL Model uses Monte Carlo simulations to calculate the cumulative fluence during a mission at a given confidence level [Fe90], [Fe93]. An example of this is shown in Figure 36 for > 30 MeV protons. Thus, according to this model, there is approximately a 10% probability of exceeding a proton fluence of 10^{10} cm⁻² for a 3-year period during solar maximum. This corresponds to a 90% confidence level that this fluence will not be exceeded.

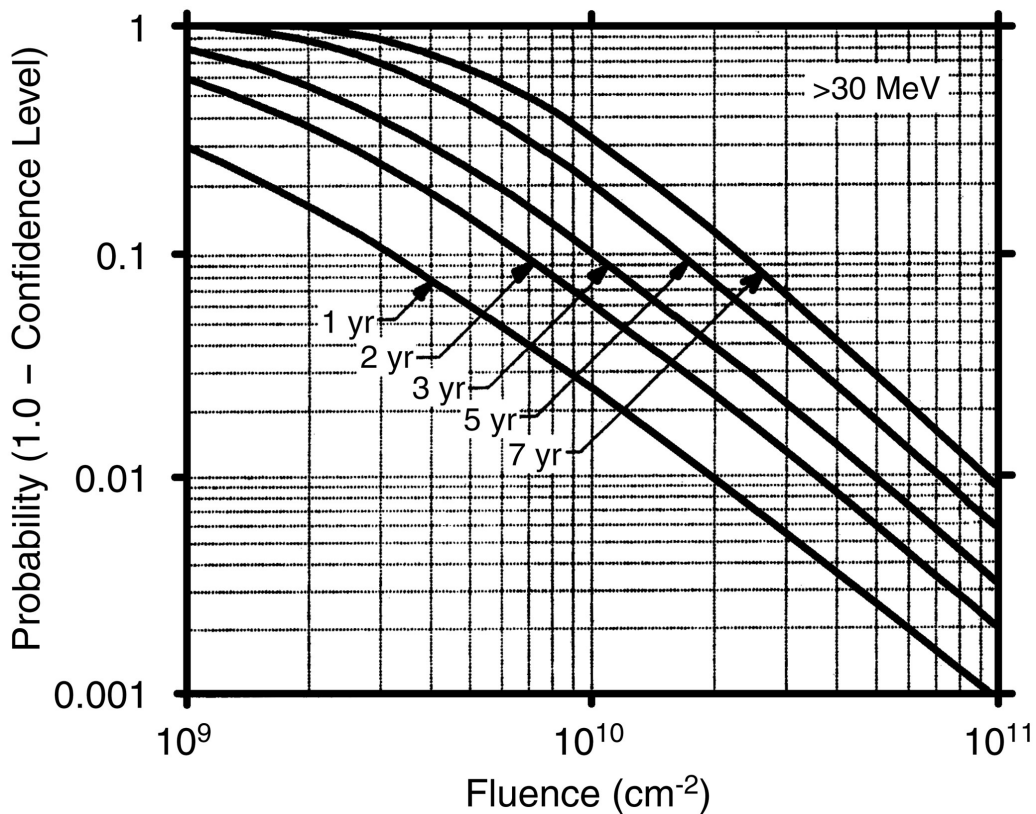


Figure 36. JPL91 solar proton fluence model for > 30 MeV protons. The misprint of x-axis units has been corrected from the original reference [Fe93].

More recently several different techniques have been used to demonstrate that the cumulative fluence distribution during solar maximum is consistent with a lognormal distribution for periods of time up to at least 7 years [Xa00]. This was shown using the Maximum Entropy Principle, Bootstrap-like methods [Ef93] and by Monte Carlo simulations using the initial distribution shown in Figure 35. Thus the cumulative fluence distribution is known once the parameters of the lognormal distribution are determined. These parameters depend on the proton energy range and the mission duration. They have been determined from the available satellite data and well-known relations for Poisson processes. Figure 37 shows examples of the annual proton fluences for >1, >10 and >100 MeV protons plotted on lognormal probability paper. This paper is constructed so that if a distribution is lognormal, it will appear as a straight line. It further illustrates that the cumulative fluences are well described by lognormal distributions. The fitted data can also be used to determine the lognormal parameters for different periods of time and is used in the ESP Model [Xa99a].

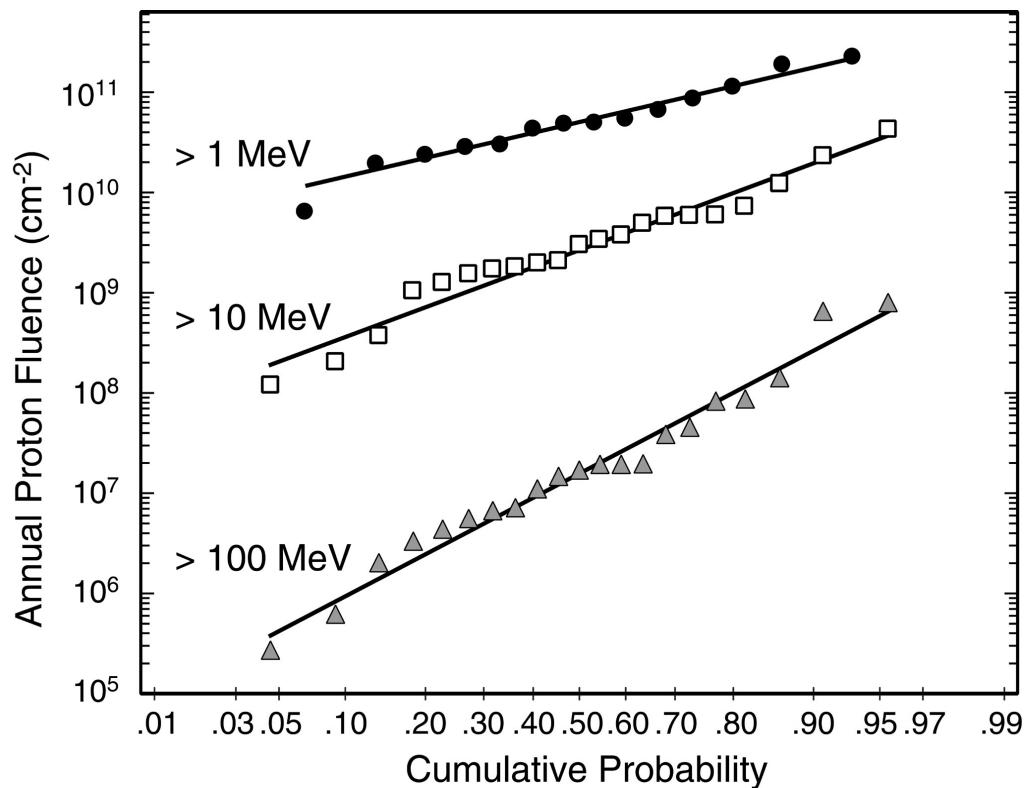


Figure 37. Cumulative annual solar proton event fluences during solar maximum periods for 3 solar cycles plotted on lognormal probability paper. The straight lines are results for the ESP model [Xa00].

Figure 38 shows a representative comparison of the models discussed above. In addition it shows an update of the ESP Model, called PSYCHIC [Xa04], in which the data were extended to cover the time period from 1966 to 2001 and the proton energy range extended to over 300

MeV. Results shown are for the 90% confidence level and for a mission length of two solar maximum years. In all cases the energy range shown corresponds to the data range on which the statistical models are based, i.e. no extrapolations are used. Thus, the model differences seen are an indicator of model uncertainties. The spectral shape for the King Model is based on the August 1972 event and is therefore somewhat different than the other model results. The JPL91, ESP, and PSYCHIC models all agree reasonably well for their common 1 to 60 MeV energy range. Note that extrapolation of the JPL91 Model beyond 60 MeV results in an overestimate of the mission fluence. A significant advantage of the PSYCHIC model is its broad energy range and incorporation of several sources of satellite data.

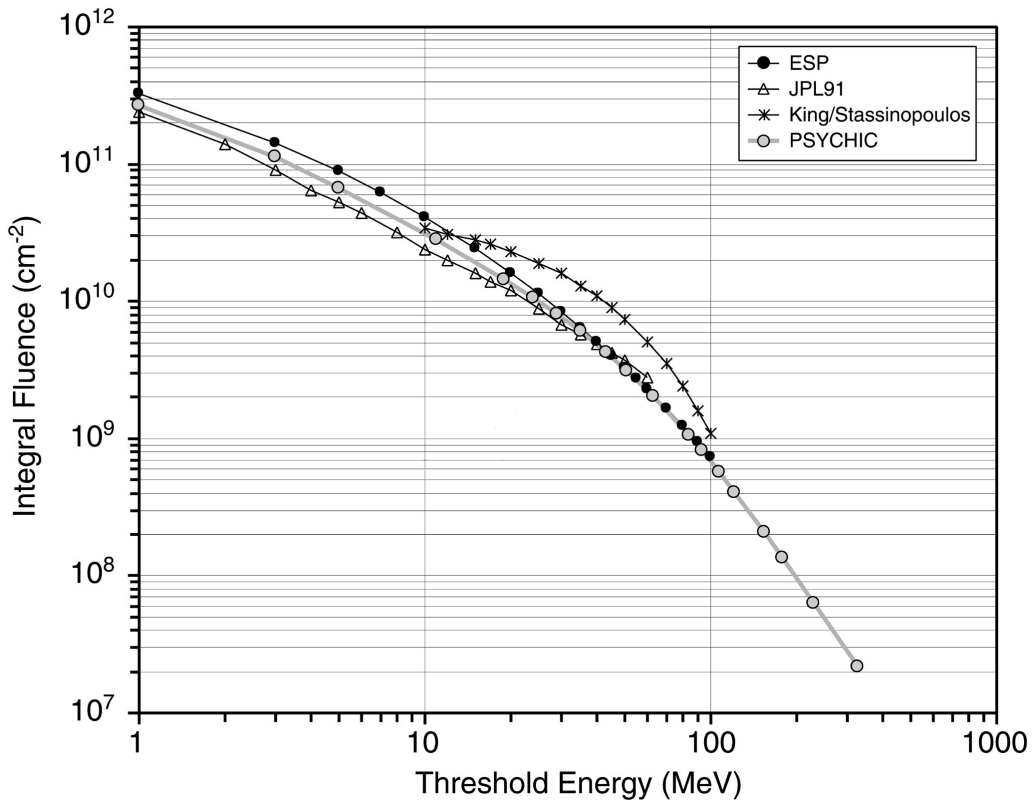


Figure 38. Comparison of different models of cumulative solar proton event fluence during solar maximum for a 2 year period and the 90% confidence level [Xa04].

3. Cumulative Fluence During Solar Minimum

It has often been assumed that the solar particle event fluence during the solar minimum time period can be neglected. However, for missions that are planned mostly or entirely during solar minimum it is useful to have guidelines for solar particle event exposures, especially considering the current frequent use of COTS microelectronics, which can exhibit rather low total dose failure levels.

Due to the relative lack of events during solar minimum, confidence level based models are difficult to construct for this period. However, recent solar minimum time periods have been analyzed to obtain 3 average solar proton flux levels that allow varying degrees of conservatism to be used [Xa04]. These flux levels are included in the PSYCHIC model and are shown in Figure 39. First there is the average flux vs, energy spectrum over all 3 solar minimum periods that occurred between 1966 and 2001. A more conservative choice is the highest flux level of the 3 periods or “worst solar minimum period”. Finally, the most conservative choice is the “worst solar minimum year”. This corresponds to the highest flux level over a one year solar minimum time period. It is the one-year interval beginning April 23, 1985 and ending April 22, 1986. Once the choice of a flux-energy spectrum is made the cumulative fluence-energy spectrum is calculated using the mission time period during solar minimum.

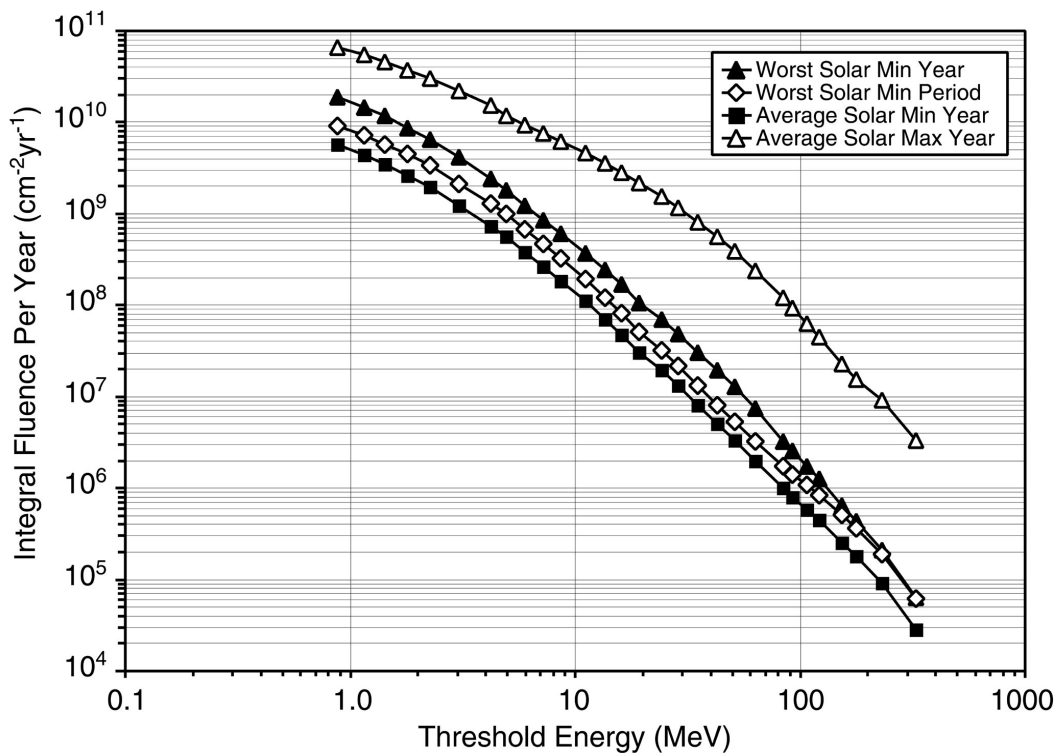


Figure 39. Solar proton flux vs. energy spectra for the 3 solar minimum model spectra in the PSYCHIC model. Also shown for comparison purposes is the average proton flux during solar maximum [Xa04].

For comparison purposes, Figure 39 also shows the average solar proton flux during solar maximum for the time period 1966 to 2001. It can be concluded that during the solar minimum time period the event frequencies are generally lower, event magnitudes are generally smaller and the energy spectra are generally softer. Physically this is consistent with the fact that the sun is in a less disturbed state during solar minimum.

4. Extreme Value Theory and Worst Case Events

An important consideration for spacecraft designers is the worst-case solar particle event that occurs during a mission. One approach is to design to a well-known large event such as that which occurred in October 1989 [Ty97], or a hypothetical one such as a composite of the February 1956 and August 1972 events [An94]. Energy spectra of some of the most severe solar proton events during solar cycles 19-22 are shown in Figure 40. In addition, there are event classification schemes in which the magnitudes range from “small” to “extremely large” that can be helpful for design purposes [St96], [Ny96].

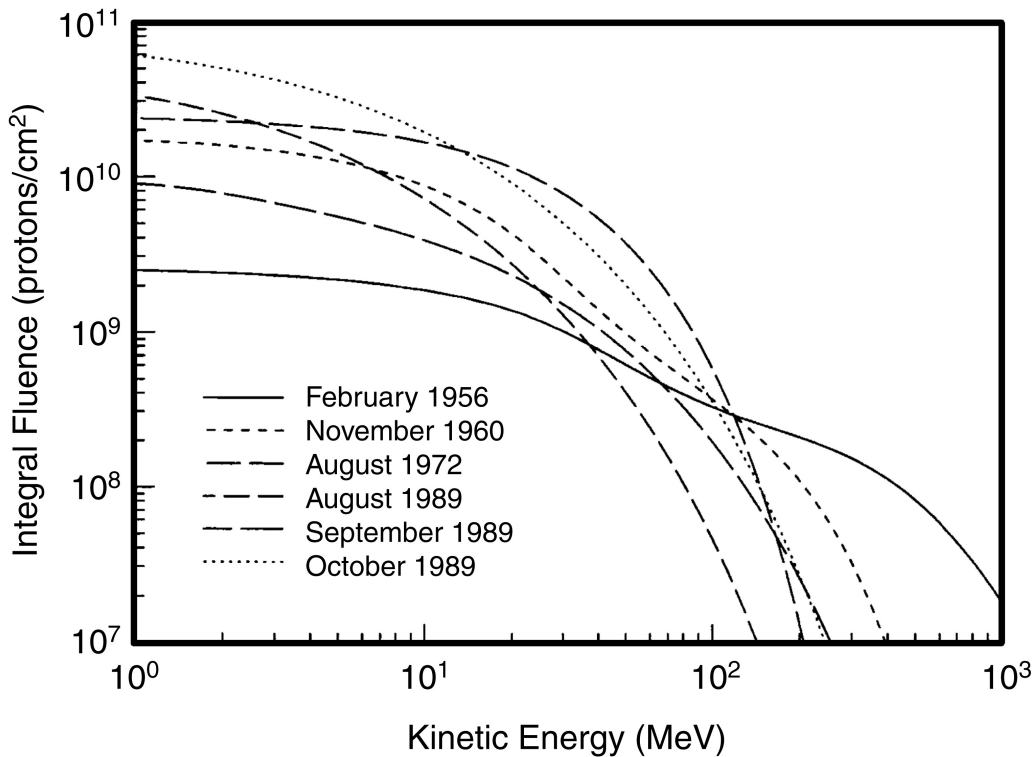


Figure 40. Some of the most severe solar proton event energy spectra in solar cycles 19-22 [Wi99].

However, more useful information can be provided to the designer if a confidence level associated with the worst case event is known for a given mission length. The designer can then more systematically balance risk-cost-performance tradeoffs for the mission in a manner similar to what is done for cumulative fluences. Once the initial probability distribution such as that shown in Figure 35 is determined it becomes possible to construct such a statistical model using extreme value theory.

In the usual central value statistics, the distribution for a random variable is characterized by its mean value and a dispersion indicator such as the standard deviation. Extreme value statistics, pioneered by Gumbel [Gu58], focuses on the largest or smallest values taken on by the distribution. Thus, the “tails” of the distribution are the most significant. For the present

applications the concern is with the largest values. An abbreviated description of a few useful relations from extreme value theory is given here. Further detail can be found elsewhere [Gu58], [An85], [Ca88].

Suppose that a random variable, x , is described by a probability density $p(x)$ and corresponding cumulative distribution $P(x)$. These are referred to as the “initial” distributions. If a number of observations, n , are made of this random variable, there will be a largest value within the n observations. The largest value is also a random variable and therefore has its own probability distribution. This is called the extreme value distribution of largest or maximum values. These probability distributions can be calculated exactly. The probability density is

$$f_{\max}(x; n) = n[P(x)]^{n-1} p(x) \quad (3)$$

and the cumulative distribution is

$$F_{\max}(x; n) = [P(x)]^n \quad (4)$$

An example of the characteristics of such a distribution is shown in Fig. 41 for n -values of 10 and 100 compared to the initial distribution ($n = 1$), taken to be Gaussian. Note that as the number of observations increase the distributions become more highly peaked and skewed to the right.

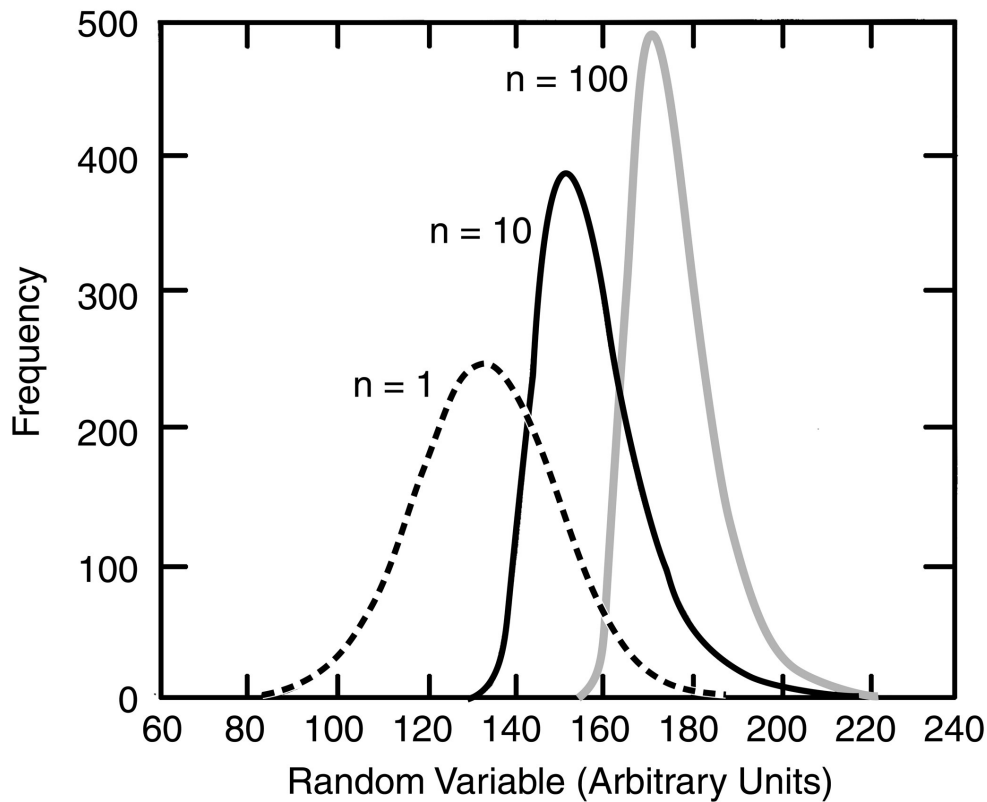


Figure 41. Extreme value distributions for n -values of 10 and 100 compared to the initial Gaussian distribution [Bu88].

As n becomes large, the exact distribution of extremes may approach a limiting form called the asymptotic extreme value distribution. If the form of the initial distribution is not known but sufficient experimental data are available, the data can be used to derive the asymptotic extreme value distribution by graphical or other methods. For practical applications there are 3 asymptotic extreme value distributions of maximum values – the type I or Gumbel , type II and type III distributions.

Examples of extreme value modeling of environmental phenomena such as floods, wave heights, earthquakes and wind speeds can be found in a number of places [Gu58], [An85], [Ca88]. This modeling was first applied to radiation effects problems by Vail, Burke and Raymond in a study of high density memories [Va83]. It has turned out to be a very useful tool for studying the response of large device arrays to radiation. One reason is that the array of devices will fail over a range of radiation exposures and it is important to determine at what point the first failure is likely to occur. Other radiation effects applications have been found for arrays of gate oxides [Va84], [Xa96], sensor arrays [Bu88], [Ma89] and EPROMs [Mc00].

For the application to solar particle events the interest is in the worst-case event that will occur over a period of T solar maximum years. Since the number of events that can occur over this period is variable, the expression for the extreme value distribution must take this into account. Assuming that event occurrence is a Poisson process [Fe93], it can be shown that the cumulative, worst case distribution for T solar maximum years is [Xa98a]

$$F_{\max}(M;T) = \exp\{-N_{\text{tot}}T[1 - P(M)]\} \quad (5)$$

where $P(M)$ is the initial cumulative distribution, which is closely related to equation (2) [Xa99].

Figure 42 shows results for worst-case event fluences for mission lengths of 1, 3, 5 and 10 solar maximum years. The ordinate represents the probability that the worst-case event encountered during a mission will exceed the > 30 MeV proton fluence shown on the abscissa. Also shown in the figure by the vertical line denoted by “Design Limit” is the maximum event fluence parameter, ϕ_{\max} . As will be discussed next, this parameter can be used as an upper limit guideline. Results analogous to these have also been obtained for peak solar proton fluxes during events [Xa98], which are very relevant for SEE. The event fluence magnitudes are discussed here because of the interesting comparison that can be made with historical data to help validate the model.

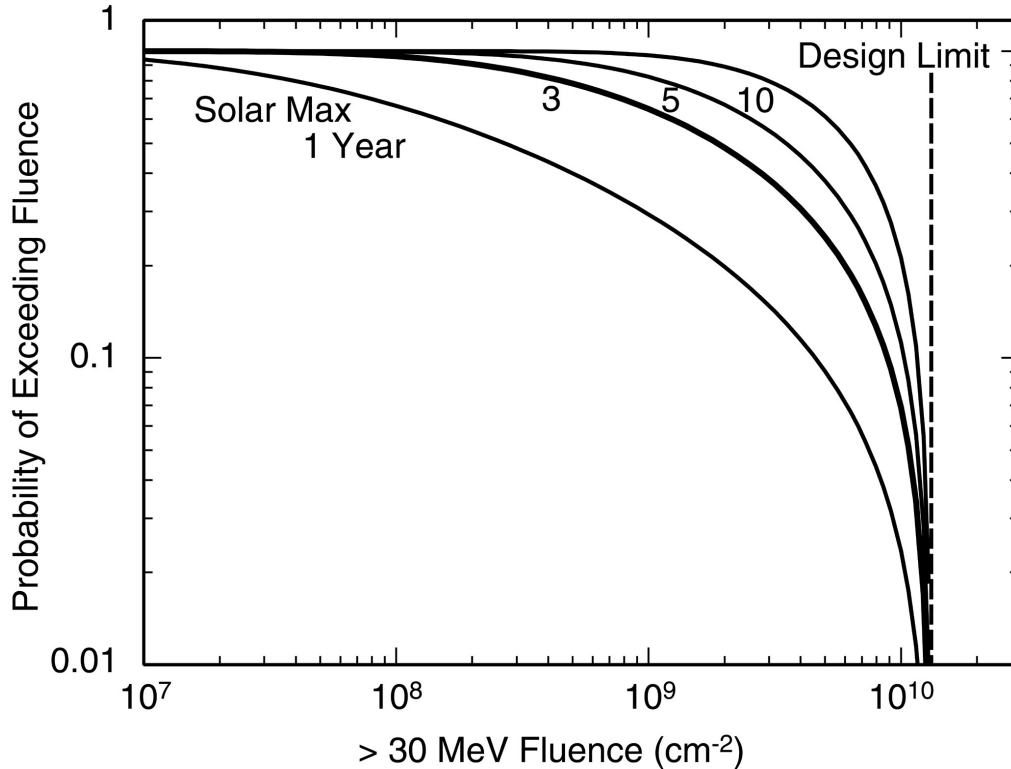


Figure 42. Probability model for worst-case event fluences expected during the indicated time periods during solar maximum [Xa99].

A unique feature of this model is the upper limit parameter for a solar proton event fluence, ϕ_{max} . For the case of > 30 MeV protons this turns out to be $1.3 \times 10^{10} \text{ cm}^{-2}$. However, this is a fitted parameter that was determined from limited data. There must be some amount of uncertainty associated with the parameter. Thus, it should not be interpreted as an absolute upper limit. One method of estimating its uncertainty is the parametric “bootstrap” technique [Ef93]. This method attempts to assess the uncertainty of the parameter due to the limited nature of the data. The idea is to randomly select event fluences according to the distribution given by equation (2) until the number of events in the distribution is simulated. The equation is then fitted to the simulated data, and the parameters extracted. The procedure is repeated, and each time the parameters have different values. After a number of simulations, the standard deviation of the parameter of interest can be determined. This technique showed the upper limit parameter plus one standard deviation equaled $3.0 \times 10^{10} \text{ cm}^{-2}$ [Xa99].

A reasonable interpretation for the upper limit fluence parameter is that it is the best value that can be determined for the largest possible event fluence, given limited data. It is not an absolute upper limit but is a practical and objectively determined guideline for use in limiting design costs.

Constraints on the upper limit of solar proton event sizes can be put on models as a result of studies of historical-type evidence. Relatively small fluctuations of ^{14}C observed in tree rings over a long period of time [Li80] and measured radioactivity in lunar rocks brought back during the Apollo missions [Re97] are consistent with the upper limit parameter but are not especially restrictive. The strictest constraint to date comes from analysis of approximately 400 years of

the nitrate record in polar ice cores [Mc01]. The largest event reported was estimated to be $1.9 \times 10^{10} \text{ cm}^{-2}$ for $> 30 \text{ MeV}$ protons. This was the Carrington event that occurred in September 1859. Fig. 43 shows a bar graph of the upper limit parameter, ϕ_{max} , for $> 30 \text{ MeV}$ protons including the one standard deviation uncertainty that was estimated from the parametric bootstrap method. This is compared with the reported value for the Carrington event. It is seen that these quantities are well within the uncertainties. Also shown for reference is the value for the October 1989 solar particle event that is commonly used as a worst-case event.

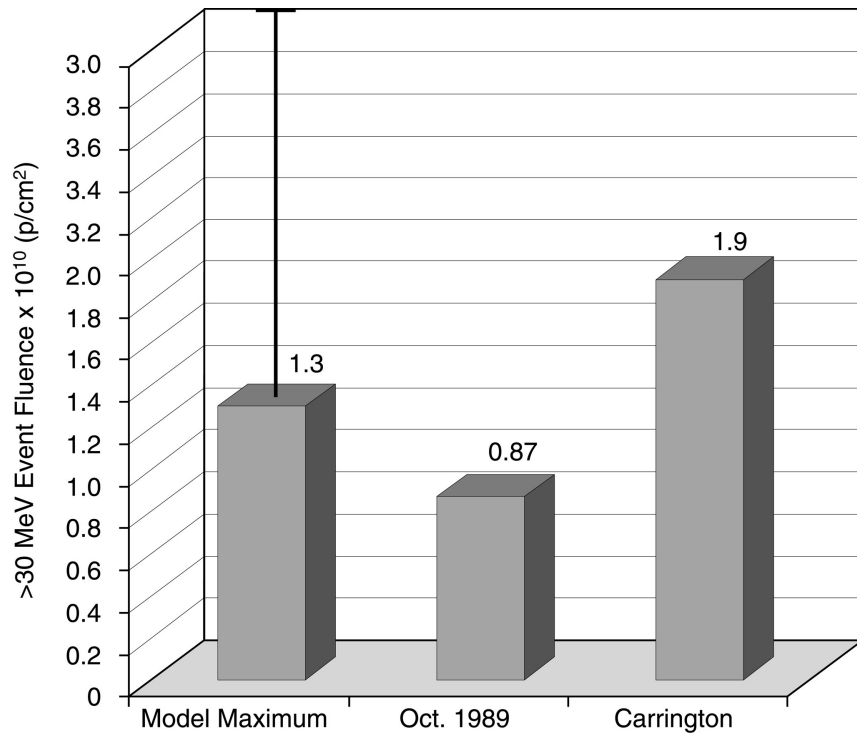


Figure 43. Comparison of the $> 30 \text{ MeV}$ solar proton event fluences of the October 1989 event, the 1859 Carrington event as determined from ice core analysis [Mc01], and the model upper limit parameter plus one standard deviation shown by the error bar [Xa99].

5. Self-Organized Criticality and the Nature of the Energy Release Process

Organizations such as NASA, ESA and others have put substantial resources into studies of the sun's properties as related to the occurrence of solar particle events. One of the main goals is to find a reliable predictor of events. Despite this significant international effort, solar particle events can occur suddenly and without obvious warning. In addition to potential problems with electronic systems and instrumentation, this is an especially serious concern for new space initiatives that plan to send manned spacecraft to the moon, Mars or interplanetary space. Thus, there is strong motivation to develop predictive methods for solar particle events. It is hoped that the apparent stochastic character can be overcome and predictability achieved if precursor phenomena such as x-ray flares or magnetic topology signatures can be properly interpreted or if the underlying mechanisms are identified. This section discusses the very basic

question of whether the nature of the energy release process for solar particle events is deterministic or stochastic. In other words is it possible to predict the time of occurrence and magnitude of solar particle events or are probabilistic methods necessary?

The self-organized criticality (SOC) model is a phenomenological model originated by Bak, Tang and Wisenfeld [Ba87] that can give insight into the basic nature of a system. It postulates that a slow continuous build-up of energy in a large interactive system causes the system to evolve to a critical state. A minor, localized disturbance can then start an energy-releasing chain reaction. Chain reactions and therefore energy releasing events of all sizes are an integral part of the dynamics, leading to a “scale invariant” property for event sizes. This scale invariance results in power function distributions for the density functions of event magnitudes and waiting times between events. As a result of this basic nature it is generally assumed in the literature that accurate predictions of the magnitude and time of occurrence of such events are not possible. A system in a SOC state is therefore generally assumed to be probabilistic in nature.

Applications for the theory of SOC have been found in natural phenomena such as earthquakes, avalanches and rainfall. A useful conceptual aid is the sandpile. If sand is dropped one grain at a time to form a pile, the pile soon becomes large enough that grains may slide down it, thus releasing energy. Eventually the slope of the pile is steep enough that the amount of sand added is balanced, on average, by the amount that slides down the pile. The system is then in the critical state. As single grains of sand are subsequently added, a broad range of consequences is possible. Nothing may happen or an avalanche of any size up to a “catastrophic” one may occur. The dynamics of this interactive system do not allow accurate predictions of when an avalanche will occur or how large it will be.

It has recently been shown that the energy release due to solar particle events is consistent with the dynamics of a SOC system [Xa06]. This was based on three analyses of 28 years of solar proton data taken by the IMP-8 and GOES series of satellites. The first is rescaled range (R/S) analysis, a method used to determine if events show long-term correlation. The second is a demonstration of fractal properties of event sizes, which suggests “scale invariant” behavior. The third is an analysis of the integral distribution of fluence magnitudes, which is shown to be a power function. These are hallmark features of systems that exhibit self-organized criticality.

a) Rescaled Range Analysis

Rescaled range (R/S) analysis, originated by Hurst [Hu65], is a method that indicates whether or not events show long-term correlation. The original goal of Hurst was to provide a basis for estimating the optimum size of water storage reservoirs. An optimum size was taken as a reservoir that never ran dry or overflowed. The analysis was based on a history of floods and droughts in the region of interest over a period of many years. For a period of years beginning at time t the cumulative input to the reservoir is

$$Y_{t+\tau} = \sum_{i=t}^{t+\tau} X_i \quad (6)$$

where the X_i are the observed inputs for a given time interval, i.e. the daily or monthly input. The cumulative deviation for the total observation period of τ years is then

$$\Delta Y_{t+\tau} = \sum_{i=t}^{t+\tau} (X_i - \overline{Y_{t+\tau}}) \quad (7)$$

where $\overline{Y_{t+\tau}}$ is the mean value of the stochastic quantity X_i . Thus, the cumulative deviation represents the difference between the actual cumulative input to the reservoir at a given time and a cumulative calculation based on the average inflow over the total time period of interest. This analysis permits identification of the maximum cumulative input and the value of the minimum cumulative store thereby enabling identification of the optimum size of the reservoir. The difference between the maximum and minimum values is customarily identified as the range.

In order to compare results for different rivers Hurst rescaled the range by dividing it by the standard deviation of the inputs over the period of the record, τ . It turns out that this rescaled range is given by

$$R/S = a\tau^H \quad (8)$$

where a and H are constants [Pe02]. The latter constant is called the Hurst coefficient. It is known that if the inputs are completely random and uncorrelated the rescaled range should vary as the square root of the elapsed time, i.e. H would equal 0.5. Contrary to this expectation Hurst found that the rescaled range varied as the 0.7 to 0.8 power of the elapsed time indicating that the events showed long-term correlation. He found that many other natural phenomena such as rainfall, temperatures, pressures and sunspot numbers had power indices in the same range.

In Figure 44 a plot analogous to that used by Hurst to describe flood and drought periods is shown for solar proton daily fluences for the year 1989. The quantity shown on the ordinate is the cumulative deviation expressed in equation (7) and can also be termed the net proton fluence. It is the analog of the reservoir level in Hurst's analysis. A negative slope on this plot indicates a lack of solar proton events (a "solar proton drought"). When an event occurs there is a rapid increase in the net proton fluence, producing the jagged appearance of the plot. This is indicative that there is a build-up of energy with time that is released in bursts.

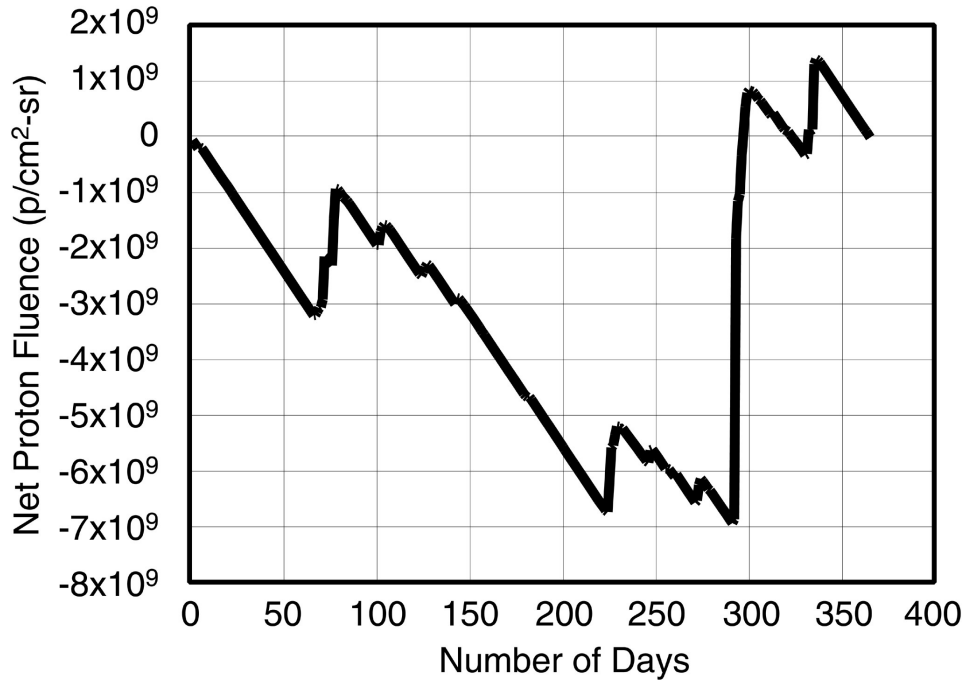


Figure 44. Cumulative deviation plot of daily solar proton fluences in 1989 [Xa06].

The difference between the maximum and minimum values in Figure 44 is conventionally referred to as the range. When divided by the standard deviation it is the rescaled range. To carry out a complete R/S analysis a number of samples covering different time periods in the total record are used to determine a series of rescaled range values. When R/S values are amenable to this analysis, they yield a straight line when plotted as a function of the period on a log-log scale. As seen in Figure 45 the solar proton data are well described by rescaled range analysis. The power index, H , has been determined using equation (8) to obtain a result of 0.70 [Xa06]. This is typical of those for other natural phenomena and indicates long-term correlation between solar particle events. This can be interpreted as a consequence of the fact that the amount of energy stored in the system, i.e. the sun's corona, is dependent on the system's past history.

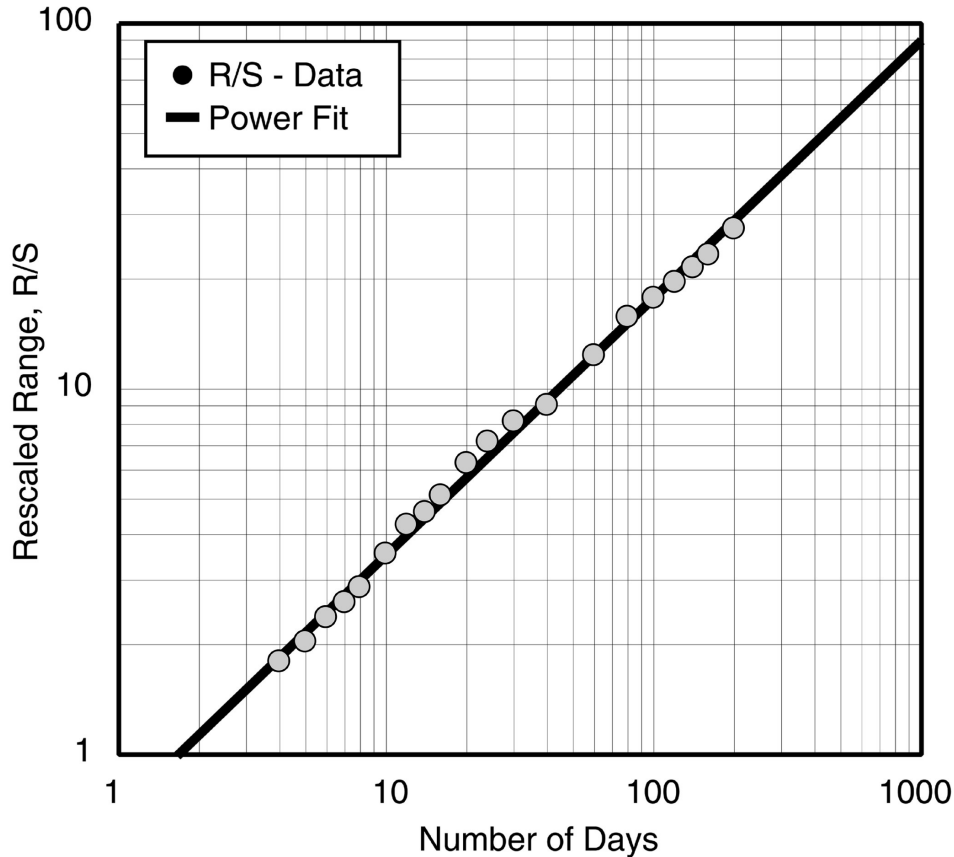


Figure 45. Rescaled range analysis of > 0.88 MeV protons for 1989 [Xa06].

b) Fractal Behavior

A significant feature of a system in a SOC state is that when its features are viewed on a different scale the character of the appearance does not change. This is closely related to Mandelbrot's concept of fractal geometry [Ma83], a formulation of the complexity of natural patterns observed in nature, which tend to have similar features regardless of the scale on which they are viewed. Well-known examples are coastlines, snowflakes and galaxy clusters.

Figure 46 shows the net proton fluence as a function of monthly fluences as compared to Figure 44, which is for daily fluences. If the axis units were not visible it would not be possible to distinguish the 2 figures. For this reason processes of this type have been described in the literature by terms such as "scale invariant", "self-similar" and "fractal" [Ba96], [Je98], [Sc91]. This scale invariance is further evidence of a SOC system, and suggests the possibility of power function behavior in the fluence magnitudes. In fact, it has been suggested that a fractal can be thought of as a snapshot of a SOC process [Ba91].

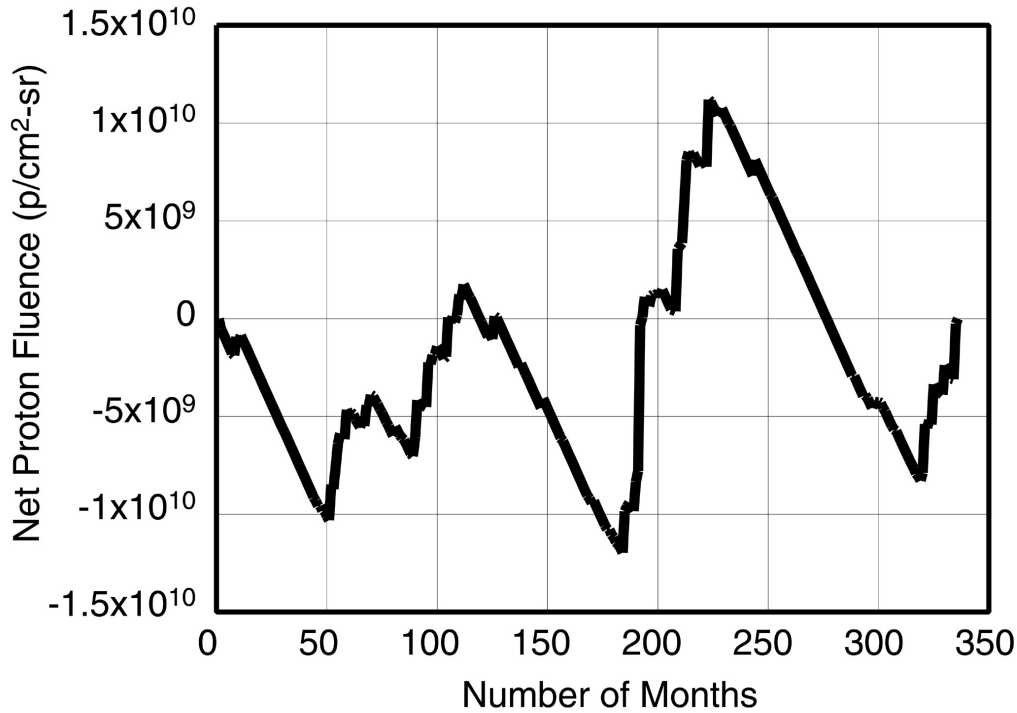


Figure 46. Cumulative deviation plot for > 0.88 MeV protons for the time period 1973 to 2001 [Xa06].

c) Power Function Distribution

A necessary characteristic of SOC phenomena is that the number density distribution of event magnitudes is a power function [Ba96], [Je98], [Pe02]. An integral distribution of monthly solar proton fluences for a 28-year period is shown in Figure 47. The ordinate represents the number of occurrences when the monthly fluence exceeds that shown on the abscissa. It is seen that this distribution is a straight line on a semi-logarithmic plot that spans about 4 orders of magnitude. The number density function is [Xa06]

$$\frac{dN}{d\Phi} = \frac{-29.4}{\Phi} \quad (9)$$

In this case the density function turns out to be exactly proportional to the reciprocal of the fluence. Thus, the solar event data can be represented by a power function of a type commonly referred to as 1/f [Ba87]. It can therefore be viewed as 1/f noise, also known as flicker noise. It is well known that this type of noise results when the dynamics of a system is strongly influenced by past events. Additionally, it reinforces the results in section B5a. Thus, an especially compelling argument can be made that solar particle events are a SOC phenomenon [Xa06].

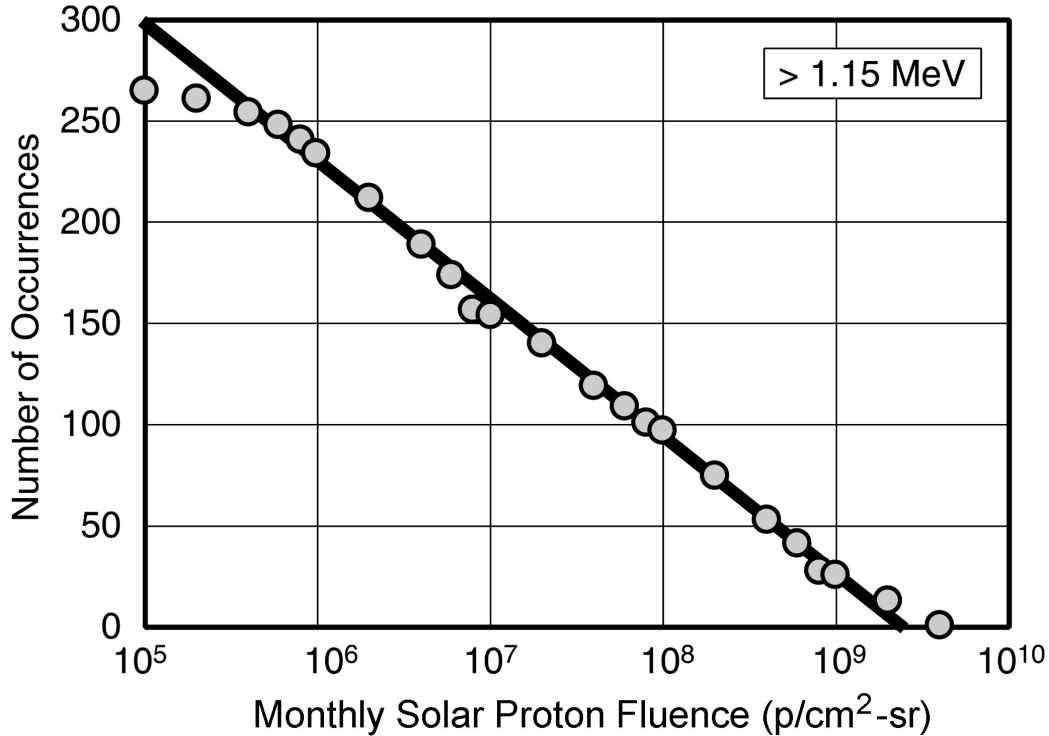


Figure 47. Integral distribution of monthly solar proton fluences > 1.15 MeV, from 1973 to 2001 [Xa06].

The general behavior of a SOC system is that of a non-equilibrium system driven by a slow continuous energy input that is released in sudden bursts with no typical size as indicated by the power function distribution shown in equation (9). Although research involving SOC is still a developing field and there is much yet to be learned about the sun's dynamics [Lu93], [Bo99], [Ga03], these results strongly suggest that it is not possible to predict that a solar particle event of a given magnitude will occur at a given time. This also suggests a direction toward a more physically based model involving a description of the energy storage and release processes in the solar structure. It is possible that such a model could explain useful probabilistic trends such as why larger and more frequent solar proton events are observed to occur during the declining phase of the solar cycle compared to the rising phase [Sh95].

C. Solar Heavy Ion Models

Solar heavy ion models are generally not as advanced as solar proton models due to the large number of heavy ion species, which complicates measurements of individual species. For microelectronics applications, solar heavy ion models are needed primarily to assess SEE. In an attempt to model worst-case events, the original CREME model [Ad87] and subsequently the CHIME model [Ch94] scaled heavy ion abundances to protons for individual events. However, this assumption that the events with the highest proton fluxes should also be heavy ion rich turned out to be inconsistent with subsequent data [Re99] and led to worst-case event models that were too conservative [Mc94]. Modifications of the original CREME code were made in the MACREE model [Ma95] to define a less conservative worst-case solar particle event. MACREE

gives the option of using a model based on the measured proton and alpha particle spectra for the well-known October 1989 event and an abundance model that is 0.25 times the CREME abundances for atomic numbers, $Z > 2$. A model that originated at JPL [Cr92] characterizes the distribution of 1 to 30 MeV per nucleon alpha particle event fluences using a lognormal distribution in order to assign confidence levels to the event magnitudes. The alpha particle data are based on measurements from the IMP-8 satellite for solar maximum years between 1973 and 1991. For ions heavier than $Z = 2$ an abundance model is used and the fluxes are scaled to the alpha particle flux for a given confidence level [Mc94]. The current version of the widely used CREME code, CREME96, uses the October 1989 event as a worst-case scenario. It provides 3 levels of solar particle intensity [Ty97]. These are the “worst week”, “worst day” and “peak flux” models, which are based on proton measurements from the GOES-6 and -7 satellites and heavy ion measurements from the University of Chicago Cosmic Ray Telescope (CRT) on the IMP-8 satellite. The most extensive heavy ion measurements in the model are for C, O and Fe ions [Ty96]. It is noteworthy that the energy spectra of these 3 elements extend out to roughly 1 GeV per nucleon. The remaining elemental fluxes are determined from a combination of measurements limited to 1 or 2 energy bins and abundance ratios.

Comparisons to the CREME96 worst case models have been made with data taken by the Cosmic Radiation Environment DOSimetry (CREDO) Experiment onboard the Microelectronics and Photonics Test Bed (MPTB) between 2000 and 2002 [Dy02]. The data show that 3 major events during this time period approximately equaled the “worst day” model. An example of this is shown in Figure 48 for an event that occurred in November 2001.

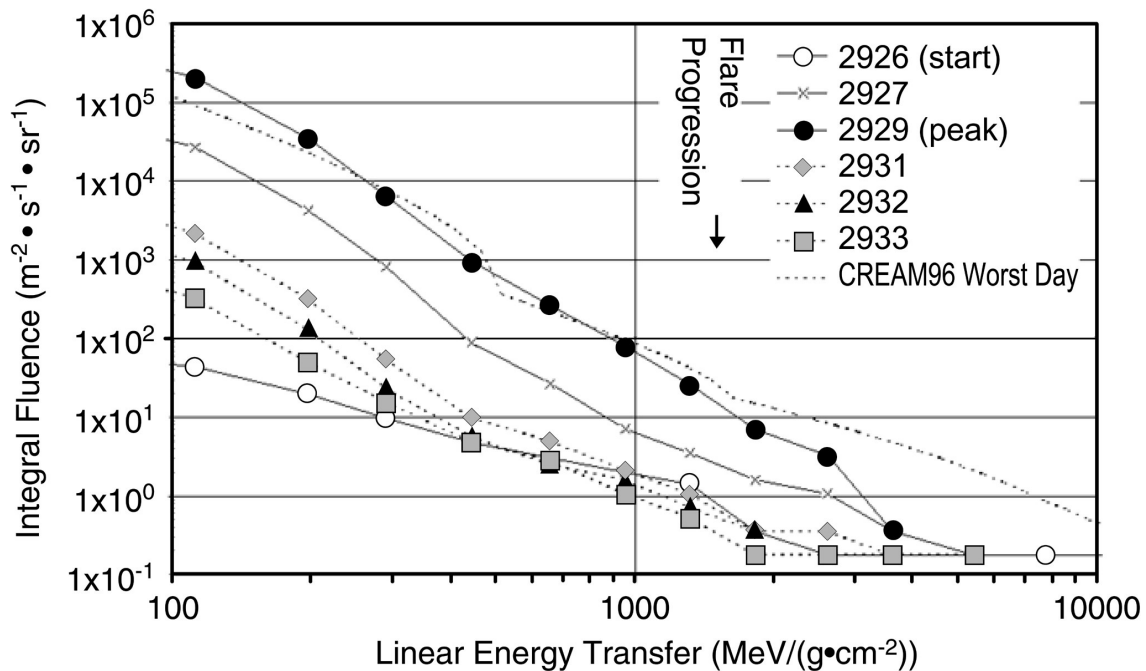


Figure 48. Comparison of a solar heavy ion event that occurred in November 2001 with the CREME96 “worst day” model. The progression of daily intensities is indicated with the peak intensity occurring on day 2929 of the mission.

The above models can be used to calculate worst-case SEE rates induced by heavy ions. Another quantity of interest is the average SEE rate during a mission, which means that models for cumulative solar heavy ion fluence must be developed. Tylka et al. used a Monte Carlo procedure similar to the JPL91 solar proton model [Fe93] to predict cumulative fluences for certain elements during a mission at a specified confidence level [Ty97a]. This was done for 2 broad energy bins each for alpha particles, for the CNO group, and for Fe. It is based on the University of Chicago CRT data taken between 1973 and 1996.

The new PSYCHIC model [Xa06a] is based on measurements of approximately 1 to 200 MeV per nucleon alpha particle data taken onboard the IMP-8 and GOES series of satellites between 1973 and 2001. For $Z > 2$ heavy ions the energy spectra and abundances relative to alpha particles are determined from measurements by the Solar Isotope Spectrometer (SIS) instrument on the ACE spacecraft for the major elements C, N, O, Ne, Mg, Si, S and Fe. These measurements were taken between 1997 and 2005. The remaining less prevalent elements are scaled according to an abundance model using the measured energy spectra of the major elements.

VI. Future Challenges

There are many future challenges that are faced in attempting to model the space radiation environment. First there should be a goal to produce more dynamical and more physical models of the environment. The resulting increased understanding should allow more accurate projections to be made for future missions. For trapped particle radiations, this would mean initially developing descriptions or particle maps for various climatological conditions that occur throughout the solar cycle for the full range of particle energies and geomagnetic coordinates covered by the AP-8 and AE-8 models. Ultimately, it would mean developing an accurate description of the source and loss mechanisms of trapped particles, including the influence that magnetic storms have on the particle populations. Galactic cosmic ray models are closely tied to solar activity levels, which modulate the fluxes of the incoming ions. Challenges for these models are to incorporate an improved description of the solar modulation potential and to develop cosmic ray transport models that incorporate knowledge of astrophysical processes. Solar particle events demonstrate a strongly statistical character. A major challenge for these models is to develop a description of the energy storage and release processes in the solar structure. This would provide a more detailed probabilistic view of the cyclical dependence of event frequencies and magnitudes.

Developing and implementing a strategy to deal with the radiation environment for manned and robotic space missions is critical for new interplanetary exploration initiatives. Getting astronauts safely to Mars and back will be the greatest exploration challenge of our lifetimes. It will involve planning and implementing strategies for the interplanetary radiation environment to an unprecedented degree. The lack of predictability of solar particle events underscores the importance of establishing a measurement system in the inner heliosphere for the early detection and warning of events [Xa06]. Once an event is detected, accurate predictions must be made of the transport process to the Earth, Mars and possibly beyond so that properties such as time of arrival, duration, intensity and energy spectrum can be transmitted well ahead of the arrival time.

The current GCR models depend on knowing the solar activity levels in order to predict GCR fluxes. Thus, the lack of an established method for predicting future solar cycle activity is a

serious concern that must be addressed for new exploration initiatives. Especially disconcerting are the occasional large drops in solar activity from one cycle to the next as seen in Figure 1. This translates to a substantial increase in GCR flux from one cycle to the next, which would be a serious problem for long-term manned missions should the mission happen to occur during an unfavorable cycle. Thus, in spite of the recent progress that has been made in modeling the space radiation environment over the last 10 or so years, much work remains to be done.

VII. References

- [Ad87] J.H. Adams, Jr., Cosmic Ray Effects on Microelectronics, Part IV, NRL Memorandum Report 5901, Naval Research Laboratory, Washington DC, Dec. 1987.
- [An85] A.H-S. Ang and W.H. Tang, *Probability Concepts in Engineering Planning and Design, Vol. II*, Wiley, NY, 1985.
- [An94] B.J. Anderson and R.E. Smith, *Natural Orbital Environment Guidelines for Use in Aerospace Vehicle Development*, NASA Technical Memorandum 4527, Marshall Space Flight Center, Alabama, June 1994.
- [An96] B.E. Anspaugh, *GaAs Solar Cell Radiation Handbook*, JPL Publication 96-9, 1996.
- [Ba96a] G.D. Badhwar and P.M. O'Neill, "Galactic Cosmic Radiation Model and Its Applications", *Adv. Space Res.*, Vol. 17, No. 2, (2)7-(2)17 (1996).
- [Ba87] P. Bak, C. Tang and K. Wisenfeld, "Self-Organized Criticality: An Explanation of 1/f Noise", *Phys. Rev. Lett.*, Vol. 59, 381-384 (1987).
- [Ba91] P. Bak and K. Chen, "Self-Organized Criticality", *Scientific American*, Vol. 264, 46-53 (Jan. 1991).
- [Ba96] P. Bak, *How Nature Works – The Science of Self-Organized Criticality*, Springer-Verlag, NY, 1996.
- [Ba97] J.L. Barth, "Modeling Space Radiation Environments" in *1997 IEEE NSREC Short Course*, IEEE Publishing Services, Piscataway, NJ.
- [Ba05] R. Baumann, "Single-Event Effects in Advanced CMOS Technology" in *2005 NSREC Short Course*, IEEE Publishing Services, Piscataway, NJ.
- [Bo99] G. Boffeta, V. Carbone, P. Giuliani, P. Veltri and A. Vulpiani, "Power Laws in Solar Flares: Self-Organized Criticality or Turbulence?" *Phys. Rev. Lett.*, Vol. 83, 4662-4665 (1999).
- [Bo03] D.M. Boscher, S.A. Bourdarie, R.H. W. Friedel and R.D. Belian, "A Model for the Geostationary Electron Environment: POLE", *IEEE Trans. Nucl. Sci.*, Vol. 50, 2278-2283 (Dec. 2003).
- [Br92] D.H. Brautigam, M.S. Gussenhoven and E.G. Mullen, "Quasi-Static Model of Outer Zone Electrons", *IEEE Trans. Nucl. Sci.*, Vol. 39, 1797-1803 (Dec. 1992).
- [Br04] D.H. Brautigam, K.P. Ray, G.P. Ginet and D. Madden, "Specification of the Radiation Belt Slot Region: Comparison of the NASA AE8 Model with TSX5/CEASE Data", *IEEE Trans. Nucl. Sci.*, Vol. 51, 3375-3380 (Dec. 2004).
- [Bu88] E.A. Burke, G.E. Bender, J.K. Pimbley, G.P. Summers, C.J. Dale, M.A. Xapsos and P.W. Marshall, "Gamma Induced Dose Fluctuations in a Charge Injection Device", *IEEE Trans. Nucl. Sci.*, Vol. 35, 1302-1306 (1988).
- [Ca88] E. Castillo, *Extreme Value Theory in Engineering*, Academic Press, Boston, 1988.

- [Ch94] D.L. Chenette, J. Chen, E. Clayton, T.G. Guzik, J.P. Wefel, M. Garcia-Munoz, C. Lopate, K.R. Pyle, K.P. Ray, E.G. Mullen and D.A. Hardy, "The CRRES/SPACERAD Heavy Ion Model of the Environment (CHIME) for Cosmic Ray and Solar Particle Effects on Electronic and Biological Systems in Space", IEEE Trans. Nucl. Sci., Vol. 41, 2332-2339 (1994).
- [Cr92] D.R. Croley and M. Cherng, "Procedure for Specifying the Heavy Ion Environment at 1 AU", JPL Interoffice Memorandum 5215-92-072, July 1992.
- [Da96] E.J. Daly, J. Lemaire, D. Heynderickx and D.J. Rodgers, "Problems with Models of the Radiation Belts", IEEE Trans. Nucl. Sci., Vol. 43, No. 2, 403-414 (April 1996).
- [Da01] A.J. Davis, et al., "Solar Minimum Spectra of Galactic Cosmic Rays and Their Implications for Models of the Near-Earth Radiation Environment", J. Geophys. Res., Vol. 106, No. A12, 29,979-29,987 (Dec. 2001).
- [Di97] E.I. Diabog, *Report on the International Workshop for Physical and Empirical Models at Dubna*, <http://wings.machaon.ru/inp50/english/dubna.html>, April 1997.
- [Di06] M. Dikpati et al., Geophys. Res. Lett. (online), March 3, 2006.
- [Dy02] C.S. Dyer, K. Hunter, S. Clucas, D. Rodgers, A. Campbell and S. Buchner, "Observation of Solar Particle Events from CREDO and MPTB During the Current Solar Maximum", IEEE Trans. Nucl. Sci., Vol. 49, 2771-2775 (2002).
- [Ef93] B. Efron and R.J. Tibshirani, *An Introduction to the Bootstrap*, Chapman & Hall, NY, 1993.
- [Fe90] J. Feynman, T.P. Armstrong, L. Dao-Gibner and S.M. Silverman, "New Interplanetary Proton Fluence Model", J. Spacecraft, Vol. 27, 403-410 (1990).
- [Fe93] J. Feynman, G. Spitale, J. Wang and S. Gabriel, "Interplanetary Fluence Model: JPL 1991", J. Geophys. Res., Vol. 98, 13281-13294 (1993).
- [Ga96] S.B. Gabriel and J. Feynman, "Power-Law Distribution for Solar Energetic Proton Events", Solar Phys., Vol. 165, 337-346 (1996)
- [Ga03] S.B. Gabriel and G.J. Patrick, "Solar Energetic Particle Events: Phenomenology and Prediction", Space Sci. Rev., Vol. 107, 55-62 (2003).
- [Gu58] E. Gumbel, *Statistics of Extremes*, Columbia University Press, NY, 1958.
- [Gu96] M.S. Gussenhoven, E.G. Mullen and D.H. Brautigam, "Improved Understanding of the Earth's Radiation Belts from the CRRES Satellite", IEEE Trans. Nucl. Sci., Vol. 43, No. 2, 353-368 (April 1996).
- [Ha99] D.H. Hathaway, R.M. Wilson and E.J. Reichmann, "A Synthesis of Solar Cycle Prediction Techniques", J. Geophys. Res., Vol. 104, A10, 22375-22388 (1999).
- [He99] D. Heynderickx, M. Kruglanski, V. Pierrard, J. Lemaire, M.D. Looper and J.B. Blake, "A Low Altitude Trapped Proton Model for Solar Minimum Conditions Based on SAMPEX/PET Data", IEEE Trans. Nucl. Sci., Vol. 46, 1475-1480 (Dec. 1999).
- [http] <http://www.spennis.oma.be/>
- [Hu65] H.E. Hurst, *Long Term Storage: An Experimental Study*, Constable & Co., Ltd., London (1965).
- [Hu98] S.L. Huston and K.A. Pfitzer, "A New Model for the Low Altitude Trapped Proton Environment", IEEE Trans. Nucl. Sci., Vol. 45, 2972-2978 (Dec. 1998).
- [Hu02] S.L. Huston, *Space Environments and Effects: Trapped Proton Model*, Boeing Final Report NAS8-98218, Huntington Beach, CA, Jan. 2002.
- [Ja57] E.T. Jaynes, "Information Theory and Statistical Mechanics", Phys. Rev., Vol. 106, 620-630 (1957).

- [Je98] H.J. Jensen, *Self-Organized Criticality*, Cambridge University Press, Cambridge, UK, 1998.
- [Ka89] J.N. Kapur, *Maximum Entropy Models in Science and Engineering*, John Wiley & Sons, Inc., NY, 1989.
- [Ki74] J.H. King, "Solar Proton Fluences for 1977-1983 Space Missions", *J. Spacecraft*, Vol. 11, 401-408 (1974).
- [Ko01] H.C. Koons, "Statistical Analysis of Extreme Values in Space Science", *J. Geophys. Res.*, Vol. 106, No. A6, 10915-10921 (June 2001).
- [La05] J-M. Lauenstein and J.L. Barth, "Radiation Belt Modeling for Spacecraft Design: Model Comparisons for Common Orbits", 2005 IEEE Radiation Effects Data Workshop Proceedings, pp. 102-109, IEEE Operations Center, Piscataway, NJ, 2005.
- [Le06] F. Lei, A. Hands, S. Clucas C. Dyer and P. Truscott, "Improvements to and Validations of the QinetiQ Atmospheric Radiation Model", Accepted for publication in *IEEE Trans. Nucl. Sci.*, June 2006 issue.
- [Li80] R.E. Lingenfelter and H.S. Hudson, "Solar Particle Fluxes and the Ancient Sun" in *Proc. Conf. Ancient Sun*, edited by R.O. Pepin, J.A. Eddy and R.B. Merrill, Pergamon Press, London, pp.69-79 (1980).
- [Lu93] E.T. Lu, R.J. Hamilton, J.M. McTiernan and K.R. Bromund, "Solar Flares and Avalanches in Driven Dissipative systems", *Astrophys. J.*, Vol. 412, 841-852 (1993).
- [Ma89] P.W. Marshall, C.J. Dale, E.A. Burke, G.P. Summers and G.E. Bender, "Displacement Damage Extremes in Silicon Depletion Regions", *IEEE Trans. Nucl. Sci.*, Vol. 36, 1831-1839 (1989).
- [Ma95] P.P. Majewski, E. Normand and D.L. Oberg, "A New Solar Flare Heavy Ion Model and its Implementation through MACREE, an Improved Modeling Tool to Calculate Single Event Effect Rates in Space", *IEEE Trans. Nucl. Sci.*, Vol. 42, 2043-2050 (1995).
- [Ma83] B.B. Mandelbrot, *The Fractal Geometry of Nature*, W.H. Freeman & Co., NY, 1983.
- [Ma99] C.J. Marshall and P.J. Marshall, "Proton Effects and Test Issues for Satellite Designers – Part B: Displacement Effects" in *1999 IEEE NSREC Short Course*, IEEE Publishing Services, Piscataway, NJ.
- [Ma02] J. Mazur, "The Radiation Environment Outside and Inside a Spacecraft" in *2002 IEEE NSREC Short Course*, IEEE Publishing Services, Piscataway, NJ.
- [Mc61] C.E. McIlwain, "Coordinates for Mapping the Distribution of Magnetically Trapped Particles", *J. Geophys. Res.*, Vol. 66, 3681-3691 (1961).
- [Mc01] K.G. McCracken, G.A.M. Dreschoff, E.J. Zeller, D.F. Smart and M.A. Shea, "Solar Cosmic Ray Events for the Period 1561 – 1994 1. Identification in Polar Ice", *J. Geophys. Res.*, Vol. 106, 21585-21598 (2001).
- [Mc94] P.L. McKerracher, J.D. Kinnison and R.H. Maurer, "Applying New Solar Particle Event Models to Interplanetary Satellite Programs", *IEEE Trans. Nucl. Sci.*, Vol. 41, 2368-2375 (1994).
- [Mc00] P.J. McNulty, L.Z. Scheick, D.R. Roth, M.G. Davis and M.R.S. Tortora, "First Failure Predictions for EPROMs of the Type Flown on the MPTB Satellite", *IEEE Trans. Nucl. Sci.*, Vol. 47, 2237-2243 (2000).
- [Ny96] R.A. Nymmik, "Models Describing Solar Cosmic Ray Events", *Radiat. Meas.*, Vol. 26, 417-420 (1996).

- [Ny96a] R.A. Nymmik, M.I. Panasyuk and A.A. Suslov, "Galactic Cosmic Ray Flux Simulation and Prediction", *Adv. Space Res.*, Vol. 17, No. 2, (2)19-(2)30 (1996).
- [Ny99] R.A. Nymmik, "Probabilistic Model for Fluences and Peak Fluxes of Solar Energetic Particles", *Radiation Measurements*, Vol.30, 287-296 (1999).
- [Pa85] E.N. Parker, "The Passage of Energetic Charged Particles Through Interplanetary Space", *Planet. Space Sci.*, Vol. 13, 9-49 (1985).
- [Pe01] W.D. Pesnell, "Fluxes of Relativistic Electrons in Low Earth Orbit During the Decline of Solar Cycle 22", *IEEE Trans. Nucl. Sci.*, Vol. 48, 2016-2021 (Dec. 2001).
- [Pe02] O. Peters, C. Hertlein and K. Christensen, "A Complexity View of Rainfall", *Phys. Rev. Lett.*, Vol. 88(1), 018701-1 (2002).
- [Re97] R.C. Reedy, "Radiation Threats from Huge Solar Particle Events", in *Proc. Conf. High Energy Radiat. Background in Space*, edited by P.H. Solomon, NASA Conference Publication 3353, pp.77-79 (1997).
- [Re99] D.V. Reames, "Particle Acceleration at the Sun and in the Heliosphere", *Space Sci. Rev.*, Vol. 90, 413-491 (1999).
- [Sa76] D.M. Sawyer and J.I. Vette, *AP-8 Trapped Proton Environment for Solar Maximum and Solar Minimum*, NSSDC/WDC-A-R&S, 76-06, NASA Goddard Space Flight Center, Greenbelt, MD, Dec. 1976.
- [Sc91] M. Schroeder, *Fractals, Chaos and Power Laws*, W.H. Freeman & Co., NY, 1991.
- [Sc96] K.H. Schatten, D.J. Myers and S. Sofia, "Solar Activity Forecast for Solar Cycle 23", *Geophys. Res. Lett.*, Vol. 6, 605-608 (1996).
- [Sh49] C.E. Shannon and W. Weaver, *The Mathematical Theory of Communication*, University of Illinois Press, 1949.
- [Sh95] M.A. Shea and D.F. Smart, "A Comparison of Energetic Solar Proton Events During the Declining Phase of Four Solar Cycles (Cycles 19-22)", *Adv. Space Res.*, Vol. 16, No. 9, (9)37-(9)46 (1995).
- [Si06] A. Sicard-Piet, S. Bourdarie, D. Boscher and R.H.W. Friedel, "A Model of the Geostationary Electron Environment: POLE, from 30 keV to 5.2 MeV", Accepted for publication in *IEEE Trans. Nucl. Sci.*, June 2006 issue.
- [St74] E. G. Stassinopoulos and J.H. King, "Empirical Solar Proton Models for Orbiting Spacecraft Applications", *IEEE Trans. Aerospace and Elect. Sys.*, Vol. 10, 442-450 (1974).
- [St96] E.G. Stassinopoulos, G.J. Brucker, D.W. Nakamura, C.A. Stauffer, G.B. Gee and J.L. Barth, "Solar Flare Proton Evaluation at Geostationary Orbits for Engineering Applications", *IEEE Trans. Nucl. Sci.*, Vol. 43, 369-382 (April 1996).
- [Tr61] M. Tribus, *Thermostatics and Thermodynamics*, D. Van Nostrand Co., Inc., NY, 1961.
- [Ty96] A.J. Tylka, W.F. Dietrich, P.R. Boberg, E.C. Smith and J.H. Adams, Jr., "Single Event Upsets Caused by Solar Energetic Heavy Ions", *IEEE Trans. Nucl. Sci.*, Vol. 43, 2758-2766 (1996).
- [Ty97] A.J. Tylka et al., "CREME96: A Revision of the Cosmic Ray Effects on Microelectronics Code", *IEEE Trans. Nucl. Sci.*, Vol. 44, 2150-2160 (1997).
- [Ty97a] A.J. Tylka, W.F. Dietrich and P.R. Boberg, "Probability Distributions of High-Energy Solar-Heavy-Ion Fluxes from IMP-8: 1973-1996", *IEEE Trans. Nucl. Sci.*, Vol. 44, 2140-2149 (1997).

- [Va83] P.J. Vail, E.A. Burke and J.P. Raymond, "Scaling of Gamma Dose Rate Upset Threshold in High Density Memories", IEEE Trans. Nucl. Sci., Vol. 30, 4240-4245 (1983).
- [Va84] P.J. Vail and E.A. Burke, "Fundamental Limits Imposed by Gamma Dose Fluctuations in Scaled MOS Gate Insulators", IEEE Trans. Nucl. Sci., Vol. 31, 1411-1416 (1984).
- [Va96] A.L. Vampola, *Outer Zone Energetic Electron Environment Update*, European Space Agency Contract Report, Dec. 1996; http://space-env.esa.int/R_and_D/vampola/text.html.
- [Ve91] J.I. Vette, *The NASA/National Space Science Data Center Trapped Radiation Environment Program (1964-1991)*, NSSDC 91-29, NASA/Goddard Space Flight Center, National Space Science Data Center, Greenbelt, MD, Nov. 1991.
- [Ve91a] J.I. Vette, *The AE-8 Trapped Electron Environment*, NSSDC/WDC-A-R&S 91-24, NASA Goddard Space Flight Center, Greenbelt, MD, Nov. 1991.
- [Wa94] M. Walt, *Introduction to Geomagnetically Trapped Radiation*, University Press, Cambridge, 1994.
- [Wa04] R.J. Walters, S.R. Messenger, G.P. Summers and E.A. Burke, "Solar Cell Technologies, Modeling and Testing" in *2004 IEEE NSREC Short Course*, IEEE Publishing Services, Piscataway, NJ.
- [Wi99] J.W. Wilson, F.A. Cucinotta, J.L. Shinn, L.C. Simonsen, R.R. Dubbed, W.R. Jordan, T.D. Jones, C.K. Chang and M.Y. Kim, "Shielding from Solar Particle Event Exposures in Deep Space", *Radiat. Meas.*, Vol. 30, 361-382 (1999).
- [Wr00] G.L. Wrenn, D.J. Rodgers and P. Buehler, "Modeling the Outer Belt Enhancements of Penetrating Electrons", *J. Spacecraft and Rockets*, Vol. 37, No. 3, 408-415 (May-June 2000).
- [Xa96] M.A. Xapsos, "Hard Error Dose Distributions of Gate Oxide Arrays in the Laboratory and Space Environments", IEEE Trans. Nucl. Sci., Vol. 43, 3139-3144 (1996).
- [Xa98] M.A. Xapsos, G.P. Summers and E.A. Burke, "Probability Model for Peak Fluxes of Solar Proton Events", IEEE Trans. Nucl. Sci., Vol. 45, 2948-2953 (1998).
- [Xa98a] M.A. Xapsos, G.P. Summers and E.A. Burke, "Extreme Value Analysis of Solar Energetic Proton Peak Fluxes", *Solar Phys.*, Vol. 183, 157-164 (1998).
- [Xa99] M.A. Xapsos, G. P. Summers, J.L. Barth, E.G. Stassinopoulos and E.A. Burke, "Probability Model for Worst Case Solar Proton Event Fluences", IEEE Trans. Nucl. Sci., Vol. 46, 1481-1485 (1999).
- [Xa99a] M.A. Xapsos, J.L. Barth, E.G. Stassinopoulos, E.A. Burke and G.B. Gee, *Space Environment Effects: Model for Emission of Solar Protons (ESP) – Cumulative and Worst Case Event Fluences*, NASA/TP-1999-209763, Marshall Space Flight Center, Alabama, Dec. 1999.
- [Xa00] M.A. Xapsos, G.P. Summers, J.L. Barth, E.G. Stassinopoulos and E.A. Burke, "Probability Model for Cumulative Solar Proton Event Fluences", IEEE Trans. Nucl. Sci., Vol. 47, No. 3, 486-490 (June 2000).
- [Xa02] M.A. Xapsos, S.L. Huston, J.L. Barth and E.G. Stassinopoulos, "Probabilistic Model for Low-Altitude Trapped-Proton Fluxes", IEEE Trans. Nucl. Sci., Vol. 49, 2776-2781 (Dec. 2002).

- [Xa04] M.A. Xapsos, C. Stauffer, G.B. Gee, J.L. Barth, E.G. Stassinopoulos and R.E. McGuire, "Model for Solar Proton Risk Assessment", IEEE Trans. Nucl. Sci., Vol. 51, 3394-3398 (2004).
- [Xa06] M.A. Xapsos, C. Stauffer, J.L. Barth and E.A. Burke, "Solar Particle Events and Self-Organized Criticality: Are Deterministic Predictions of Events Possible?", Accepted for publication in IEEE Trans. Nucl. Sci., June 2006 issue.
- [Xa06a] M.A. Xapsos et al., submitted to the 2006 NSREC (Ponte Vedra Beach, FL).